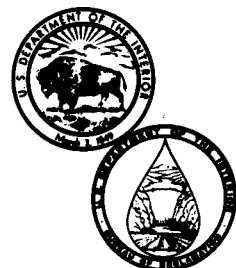


# **DYNAMIC EFFECTIVE STRESS FINITE ELEMENT ANALYSIS OF DAMS SUBJECTED TO LIQUEFACTION**

**December 1986**

**Engineering and Research Center**

**Department of the Interior  
Bureau of Reclamation**



1. REPORT NO. REC-ERC-86-4		3. RECIPIENT'S CATALOG NO.	
4. TITLE AND SUBTITLE Dynamic Effective Stress Finite Element Analysis of Dams Subjected to Liquefaction		5. REPORT DATE December 1986	
		6. PERFORMING ORGANIZATION CODE D-230	
7. AUTHOR(S) David W. Harris		8. PERFORMING ORGANIZATION REPORT NO. REC-ERC-86-4	
9. PERFORMING ORGANIZATION NAME AND ADDRESS Bureau of Reclamation Engineering and Research Center Denver, CO 80225		10. WORK UNIT NO.	
		11. CONTRACT OR GRANT NO.	
12. SPONSORING AGENCY NAME AND ADDRESS Same		13. TYPE OF REPORT AND PERIOD COVERED	
		14. SPONSORING AGENCY CODE DIBR	
15. SUPPLEMENTARY NOTES Microfiche and/or hard copy available at the E&R Center, Denver, Colorado  <p style="text-align: right;">Editor:RNW(c)</p>			
16. ABSTRACT The demand for safe facilities, especially those of great sensitivity and importance such as large embankment dams, nuclear powerplants, and offshore structures, has affirmed the need for improved analysis tools for evaluating their load-deformation responses and strength behavior, especially in earthquake-prone regions.  The dynamic stress-strain, strength, and pore water pressure behavior of water-saturated soils in embankment dams and their foundations is highly nonlinear and quite difficult to model in a realistic manner. This report presents a simplified nonlinear finite element analysis technique that incorporates many of the important features of more rigorous procedures, yet requires input parameters that can be obtained from standard laboratory tests. Thus, it can be applied to predict the complex load-deformation and pore water pressure behavior of large dams. Analyses of established field cases show that the technique is feasible as a working tool. The analysis algorithm is based on an uncoupled relationship between soil skeleton deformations and pore water pressure as opposed to the coupled equations used in Biot-analysis. Comparisons between analytical predictions and laboratory and field experience show that the procedure is quite satisfactory.			
17. KEY WORDS AND DOCUMENT ANALYSIS a. DESCRIPTORS-- finite element/ *liquefaction/ dynamic/ constitutive models/ pore pressure/ stress/ strain/ earthquakes  b. IDENTIFIERS-- Upper San Fernando Dam/ Lower San Fernando Dam  c. COSATI Field/Group 08M 20K COWRR: 2011 0813 SRIM:			
18. DISTRIBUTION STATEMENT Available from the National Technical Information Service, Operations Division, 5285 Port Royal Road, Springfield, Virginia 22161.  (Microfiche and/or hard copy available from NTIS)		19. SECURITY CLASS (THIS REPORT) UNCLASSIFIED	21. NO. OF PAGES 45
		20. SECURITY CLASS (THIS PAGE) UNCLASSIFIED	22. PRICE



92023147

**REC-ERC-86-4**

**DYNAMIC EFFECTIVE STRESS  
FINITE ELEMENT ANALYSIS OF  
DAMS SUBJECTED TO LIQUEFACTION**

by

**David W. Harris**

**December 1986**

Embankment Dams Branch  
Division of Dam and Waterway Design  
Engineering and Research Center  
Denver, Colorado

## ACKNOWLEDGMENTS

Major portions of the text are extracted from the author's thesis entitled "A Simplified Nonlinear Effective Stress Finite Element Analysis Procedure for Embankment Dams Subjected to Dynamic Loading," available from University Microfilms, Ann Arbor, Michigan. During the preparation of this thesis, review comments and guidance were given by Professors Sture and Ko. The text was prepared by the Word Processing Center at the Bureau of Reclamation's Engineering and Research Center.

As the Nation's principal conservation agency, the Department of the Interior has responsibility for most of our nationally owned public lands and natural resources. This includes fostering the wisest use of our land and water resources, protecting our fish and wildlife, preserving the environmental and cultural values of our national parks and historical places, and providing for the enjoyment of life through outdoor recreation. The Department assesses our energy and mineral resources and works to assure that their development is in the best interests of all our people. The Department also has a major responsibility for American Indian reservation communities and for people who live in Island Territories under U.S. Administration.

The information contained in this report regarding commercial products or firms may not be used for advertising or promotional purposes and is not to be construed as an endorsement of any product or firm by the Bureau of Reclamation.

# CONTENTS

	Page
Glossary of symbols .....	v
Purpose .....	1
Introduction.....	1
Material models including pore pressure effects .....	2
Hyperbolic model.....	2
Weidlinger cap model.....	3
Yield surface .....	4
Flow rule .....	6
Hardening rule.....	6
Evaluating parameters for the Weidlinger cap model.....	7
Pore pressure model.....	7
Determination of material constants .....	10
Cyclic triaxial test prediction.....	12
Dams subjected to earthquakes.....	12
Oroville Dam.....	12
Sheffield Dam.....	14
Lower San Fernando Dam .....	17
Upper San Fernando Dam.....	24
Conclusions .....	25
Bibliography .....	35
Appendixes	
A – Typical hyperbolic model constants for dams.....	37
B – Calculations of cap parameters for Oroville Dam .....	43

## TABLES

### Table

1	Cyclic triaxial test results – Sample No. B2-100-2 .....	29
2	Cyclic triaxial test results – Sample No. B2-100-3 .....	29
3	Cyclic triaxial rest results – Sample No. B2-100-4 .....	29
4	Cyclic triaxial test results – Sample No. B2-100-5 .....	30
5	Cyclic triaxial test results – Sample No. B2-100-6 .....	31
6	Oroville Dam strength parameters.....	31
7	Sheffield Dam strength parameters .....	32
8	Lower San Fernando Dam strength parameters.....	33
9	Upper San Fernando Dam strength parameters.....	34
A.1	Hyperbolic parameters for drained conditions .....	39
A.2	Hyperbolic parameters for undrained conditions .....	41

## FIGURES

### Figure

1	Hyperbolic stress-strain curve .....	3
2	Example stress – strain curve showing unloading .....	4
3	Calculation sheet for $E_t, B_t$ parameters .....	5
4	Ultimate strength and yield surfaces with cap model.....	5

## CONTENTS – Continued

Figure

Page

5	Effect of $R$ on undrained strain path.....	8
6	Simple cyclic shear strain test.....	8
7	Plot of typical cyclic strain data.....	9
8	Plot of $\Delta u/\sigma'_{vo}$ vs. $\zeta$ for cyclic strain data.....	9
9	Plot of $\Delta u/\sigma'_{vo}$ vs. $\kappa$ for cyclic strain data ( $\lambda = \text{constant}$ ).....	10
10	Plot of $\Delta u/\sigma'_{vo}$ vs. $\kappa$ for cyclic strain data ( $\lambda = \text{variable}$ ).....	11
11	Plot of $\Delta u/\sigma'_{vo}$ vs. $\zeta$ for cyclic triaxial data.....	12
12	Plot of $\Delta u/\sigma'_{vo}$ versus $\kappa$ for cyclic triaxial data.....	13
13	Cyclic triaxial test idealization.....	14
14	Hyperbolic cyclic triaxial results.....	15
15	Cap model cyclic triaxial results.....	16
16	Maximum cross section and earthquake record of Oroville Dam.....	17
17	Comparison of stress results using construction layers and gravity turn on.....	18
18	Comparison of computed and measured crest accelerations.....	18
19	Cross section and earthquake record of Sheffield Dam.....	19
20	Hyperbolic prediction for time 0.505 second – Sheffield Dam.....	20
21	Hyperbolic prediction for time 0.530 second – Sheffield Dam.....	20
22	Hyperbolic prediction for time 0.630 second – Sheffield Dam.....	20
23	Displacement vectors for hyperbolic prediction at time 0.630 second – Sheffield Dam.....	20
24	Model of liquefaction progression for Sheffield Dam.....	21
25	Cap model prediction for time 0.405 second – Sheffield Dam.....	21
26	Cap model prediction for time 0.430 second – Sheffield Dam.....	21
27	Displacement vectors for cap model prediction at time 0.430 second – Sheffield Dam.....	21
28	Maximum cross section and earthquake record of Lower San Fernando Dam.....	22
29	Interpretation of the Lower San Fernando Dam failure.....	23
30	Hyperbolic prediction with interpreted failure – Lower San Fernando Dam.....	24
31	Displacement vectors for hyperbolic prediction – Lower San Fernando Dam.....	25
32	Cap prediction with interpreted failure.....	25
33	Displacement vectors for cap model – Lower San Fernando Dam.....	25
34	Maximum cross section and earthquake record of Upper San Fernando Dam.....	26
35	Hyperbolic prediction for time 0.13 second – Upper San Fernando Dam.....	27
36	Hyperbolic prediction for time 0.18 second – Upper San Fernando Dam.....	27
37	Cap prediction for time 0.705 second – Upper San Fernando Dam.....	27
38	Cap prediction for time 2.955 seconds – Upper San Fernando Dam.....	28
39	Displacement vectors for cap model – Upper San Fernando Dam.....	28

## GLOSSARY OF SYMBOLS

$A, B, C$	Material constants
$A_u, B_u$	Pore pressure constants
$B_i$	Initial bulk modulus
$B_t$	Bulk modulus
$b$	$(J_{2D})^{1/2}$ value when $J_1 = L$
$b_H$	Asymptote of hyperbola of stress-strain curve
$[C]$	Coefficient matrix for stress-strain relationship
$C^{e-p}$	Coefficient matrix for elastic-plastic analysis
$c$	Cohesion
$D$	Hardening parameter
$D_r$	Relative density
$E_i$	Initial Young's modulus
$E_t$	Tangent Young's modulus
$e_{ij}$	Deviatoric total strain tension
$E_{ur}$	Unloading-reloading modulus
$f_c$	Function which expresses capped surface
$f_f$	Function which expresses yield surface
$g$	Gravitational constant
$G$	Modulus of rigidity
$J_1$	First stress invariant
$J_{2D}$	Second invariant of stress deviator
$K$	Stiffness coefficient for Young's modulus
$K_b$	Coefficient for bulk modulus
$K_o$	Uniaxial strain
$K_{ur}$	Coefficient for loading and unloading modulus
$k$	Soil cohesion parameter
$L$	Value of $J_1$ where elliptical surface intersects the ultimate strength surface
$m$	Exponent for bulk modulus
$n$	Exponent for Young's modulus
$p$	Superscript denoting plastic component
$p_a$	Atmospheric pressure
$R$	Ratio of major and minor axis of the surface ellipse
$R_f$	Ratio of failure stress to asymptotically smaller values at lower strain
$S$	An internal state variable that characterizes the hardening process
$T$	Transformation constant
$t$	Time
$u$	Pore pressure
$u_o$	Initial pore pressure
$u_t$	Accumulated pore pressure
$V$	Volume
$W$	Hardening parameter
$X$	Value of $J_1$ where the elliptical surface intersects the $J_1$ axis
$X_{int}$	Initial position of elliptical surface
$\alpha$	Soil friction parameter
$\gamma, \gamma_1, \gamma_2$	Cyclic shear strain
$\gamma_b$	Buoyant unit weight
$\gamma_d$	Dry unit weight
$\gamma_{max}$	Maximum shear strain
$\gamma_{oct}$	Octahedral shear strain

## GLOSSARY OF SYMBOLS – Continued

$\varepsilon$	Strain
$\varepsilon_a$	Strain in axial direction
$\varepsilon_x$	Strain in global x direction
$\varepsilon_y$	Strain in global y direction
$\varepsilon_z$	Strain in global z direction
$\varepsilon_{yz}$	Shear strain
$\varepsilon_{ij}$	Strain tensor
$\varepsilon_{ij}^e$	Elastic strain tensor
$\varepsilon_{ij}^p$	Plastic strain tensor
$\varepsilon_v^p$	Plastic volumetric strain
$\kappa$	Strain damage parameter
$\lambda$	Pore pressure constant
$\nu$	Poisson's ratio
$\xi$	Strain path parameter
$\zeta$	Strain path length
$\sigma$	Stress
$\sigma'$	Effective stress
$\sigma_1$	Axial stress
$\sigma_2$	Intermediate stress
$\sigma_3$	Confining stress
$\sigma_d$	Cyclic deviator stress
$\sigma_{ij}$	Stress tensor
$\sigma_r$	Radial stress
$\sigma_t$	Total stress
$\sigma_{vo}'$	Applied confining stress
$\sigma_z$	Stress in global z direction
$\tau$	Shear stress
$\varphi$	Internal angle of friction

## PURPOSE

This report describes a nonlinear finite element method for predicting liquefaction and deformations in embankment dams and their foundations. Two constitutive models: (1) the hyperbolic model and (2) the Weidlinger cap model (plasticity model) are discussed. An endochronic pore pressure model based on straining of material is used to predict pore pressure buildup. Acceleration time histories may be applied to the base of the finite element mesh to provide earthquake loadings. Analysis results provide accelerations, displacements, stresses, and pore pressures throughout the mesh. Both total and effective stress paths are reported for any given time step. Failure of material is modeled both by soil strength parameters and by the onset of excess pore pressures. Thus, the deformation of dams may be calculated with a single analysis technique. Liquefaction may be predicted and deformation calculated with this failure mode.

## INTRODUCTION

The state of the art of soil dynamics and geotechnical earthquake engineering analysis procedures were reviewed by Lysmer [15] in 1978. He summarized his assessment of current knowledge and the techniques for considering dynamic analyses of earth structures and soil-structure interaction problems as:

“Having taken a sober look at the possibilities for nonlinear analysis and with this the dream of all soils engineers, dynamic effective stress analysis with evaluation of dynamic pore pressures, you might conclude with the writer that the state-of-the-art of dynamic analysis is still in its infancy and that for a long time to come most soil dynamics problems will have to be solved by total stress analysis and essentially linear methods of analysis.”

Well-behaved finite element analysis codes are still scarce. It is very difficult to devise generally applicable constitutive models that account for the nonlinear, load-path dependent, inelastic and dilatant behavior of soils. It becomes equally difficult to implement these models in dynamic analysis computer codes. At the present time, detailed numerical analysis studies of earth embankment and foundation conditions are often limited by the size of the problem, uncertainties in material behavior, pore water pressure generation and distribution mechanisms, and material and geometric nonlinearities. Currently, employed analysis techniques, such as linear and equivalent linear solutions in the frequency and time domain, are well documented in the literature.

Material models that incorporate and realistically model load reversals and pore pressure changes caused by dynamic or cyclic loading, that are simple to implement and use, and that require easily obtainable material properties are still not available as a pragmatic design tool. The methods discussed in this report attempt to bridge this gap and to present the development of a practical computational analysis code based on effective stress concepts. This report contains a description of the implemented theory, the calculation of necessary properties and values for input, and a verification of its utility by applying the code both on known experimental results and on actual documented field cases.

Earthquakes, in general, pose a severe loading condition for embankment dams. Thus, although it is important to perform static analyses, it is more important to analyze and understand the dynamic behavior of dams and to predict whether or not failure is impending under the anticipated worst-case loadings. Many of the dams that have been built in different parts of the world over the past 5,000 years have been subjected to earthquakes with varied results [11]. Some dams have suffered little or no damage but others have failed.

To predict the wide range of performance in dams, traditional analyses have generally been developed in two different categories for predicting failure: (1) excessive displacement during shaking and (2) liquefaction of the dam and/or foundation and a subsequent complete loss of the dam section. The two categories differ with respect to the amount and type of strain that occurs, the loading necessary for its use, and the effects of various parameters on these phenomena [20, 9].

Displacements can occur in instances of gradually increasing cyclic strains without complete loss in shear strength and stiffness, or cyclic mobility. Cyclic mobility has been used to explain progressive stiffening and weakening under cyclic loading on relatively dense sandy soil. Liquefaction, on the other hand, is a result of high excess pore water pressures and the subsequent loss of strength and stiffness caused by a loose, contractive soil structure. Despite a few controversial issues related to the general terminology and the origin and evaluation of certain liquefaction mechanisms, there appears to be general agreement in the geotechnical engineering community about (1) the importance of understanding the dynamic stress, strain, strength, and pore water pressure behaviors of soils, (2) the importance of knowing the liquefaction potential of subsoils in earthquake-prone regions, and (3) the need for pursuing further research in these areas. In fact, to quote the 1983 report *Safety of Existing Dams* [16] by the National Research Council, “To evaluate the stability

of loose cohesionless materials, . . . realistic dynamic analyses should be used in conjunction with special laboratory tests to evaluate soil strength under cyclic loading." Both categories are difficult to model analytically because of the complex nature of typical soil behavior that accounts for nonlinearity, dilatancy, and other complex phenomena. Traditional methods that were previously available have required significant simplifying assumptions and are generally used to simulate either cyclic mobility or liquefaction.

The system of equations used in this solution employs the mass and acceleration of the dam, the nonlinear stiffness of the dam, and a forcing function. A multisurface plasticity model was used to generate the hysteretic yielding behavior of the materials. For this case, the soil damping is independent of the strain rate and is modeled accurately in an implicit manner without the use of an explicit damping term in the governing equation. This eliminates the need to derive damping characteristics and solve equations with complex solutions. The material constants needed are found from standard triaxial tests. This type of analysis, which is reasonable for problems of practical relevance, is far less expensive than more complex formulations.

To be useful as a predictive tool, models must be capable of handling problems with complex geometries, complicated loading situations, and typical soil responses. One class of methods used to accomplish this verification is laboratory experimentation, such as performed in triaxial tests. These tests are normally used to establish soil properties and can be used as an example to verify the correctness of the implementation of the numerical model. However, triaxial tests represent a single element of a soil mass and are not sufficient proof of the problem-solving capability relative to field cases. Four known field cases represent a full range of possible failure mechanisms in dams:

1. Oroville Dam – a significant earthquake event that had no effect on the dam
2. Sheffield Dam – a liquefaction failure with loss of the dam
3. Lower San Fernando Dam – a liquefaction failure with a near loss of the dam
4. Upper San Fernando Dam – a displacement failure of the dam

These cases are studied using analysis methods described in this report. Published material properties are used and only a single analysis was conducted to predict behavior; no attempt was made to vary the input constants in an iterative manner until results matched the known field behavior. The results are discussed together with comparisons of methods and conclusions.

It has been estimated (by Peck [17]) that the probability of a catastrophic failure of a major dam during any given year is about 1 in 10,000. Stated in perhaps a more pragmatic way, 1 in every 100 dams will fail in a lifetime of 100 years. The understanding and consideration of the factors that affect dam failures can be used to decrease this probability. Methods presented in this report can be used to model nonlinear soil behavior, complex cyclic loading and unloading conditions encountered during applied earthquake loading, and pore pressures generated. All of these properties are modeled simultaneously, which provides a complete tool for the effective stress analysis and the prediction of possible failure modes in embankment dams or other soil structures. Thus, such analyses can be used effectively to increase the safety of dams through necessary modifications.

## MATERIAL MODELS INCLUDING PORE PRESSURE EFFECTS

Two models from the literature are chosen for this study and implemented in an existing finite element computer code, ADINA/BM [2]. An endochronic pore pressure is used in conjunction with these models. A brief description of the derivation and assumptions of the models and the calculation of the appropriate input constants are covered in each of the following sections.

### Hyperbolic Model

The hyperbolic model is an early model used in the finite element method. It is one of the most common models used today in the analysis of soil mechanics problems. The hyperbolic model was first proposed for static and monotonic loading by K ondner [13] and was implemented by Duncan and Chang [7] for finite element analysis. The stress – strain response curve is assumed to closely represent a hyperbola, as shown on figure 1. This assumed property may be combined with the Mohr-Coulomb failure criterion to express a relationship between compressive strength and confining stress in the form of a tangent modulus,  $E_t$ , as:

$$E_t = \left[ 1 - \frac{R_f (1 - \sin \phi) (\sigma_1 - \sigma_3)}{2c \cos \phi + 2\sigma_3 \sin \phi} \right]^2 K p_a \left( \frac{\sigma_3}{p_a} \right)^n \quad (1)$$

The bulk modulus may be given as a function of confining pressure [10] as:

$$B_t = K_b p_a (\sigma_3 / p_a)^m \quad (2)$$

A tangent stress-strain relationship using the values of  $E_t$  and  $B_t$  may be given as:

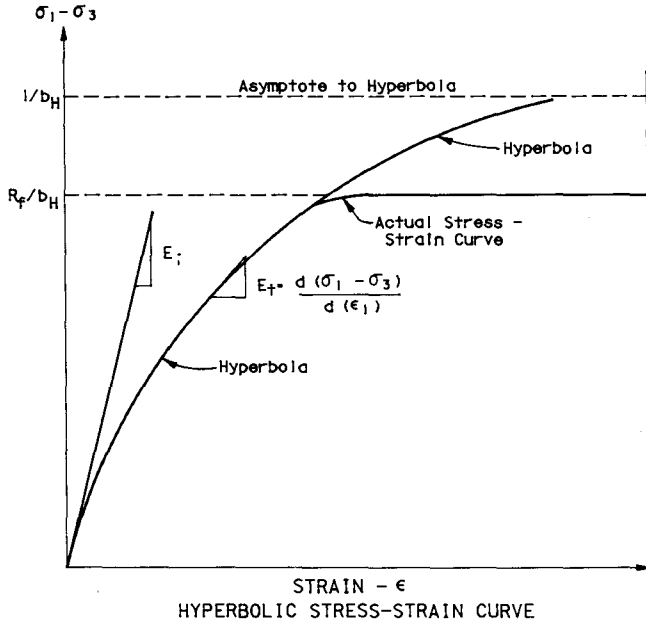


Figure 1. - Hyperbolic stress-strain curve. From [12].

$$[C] = \frac{3E_t}{9B_t - E_t} \begin{bmatrix} 3B_t + E_t & 3B_t - E_t & 0 \\ 3B_t - E_t & 3B_t - E_t & 0 \\ 0 & 0 & E_t \end{bmatrix} \quad (3)$$

The unloading and reloading moduli are generally taken as constant modulus values. The modulus can be related to confining pressure as:

$$E_{ur} = K_{ur} (p_a) \left( \frac{\sigma_3}{p_a} \right)^n \quad (4)$$

Determining when a soil element in a field problem is unloading requires a general algorithmic expression. It cannot be based on confining pressure or axial loading alone. As can be seen on figure 2, careful consideration must be given to this procedure. An incorrect choice of the unloading and reloading modulus can follow a path that creates or adds energy to the system and, therefore, will create an incorrect physical approximation causing numerical instability in the solution. Various alternatives on which to base the procedure are available: (1) an expression or decision algorithm to determine the most prevalent effect, (2) energy calculations to ensure that energy is not being added to the system by the unloading-reloading process, and (3) evaluation of plastic strains. The expression used to determine unloading in the implemented model is the octahedral shear strain, which is defined as:

$$\gamma_{oct} = \frac{2}{3} [(\epsilon_x - \epsilon_y)^2 + (\epsilon_y - \epsilon_z)^2 + (\epsilon_z - \epsilon_x)^2 + \frac{3}{2} \epsilon_{yz}^2]^{1/2} \quad (5)$$

This expression is chosen because shear strains in this model are unaffected by pore water pressures or by hydrostatic total stress changes. Strains are calculated directly from displacements, thus eliminating iterations for stress using the material law. Increasing octahedral shear strain identifies loading; whereas, decreasing octahedral shear strain identifies unloading. The unloading-reloading modulus is used during an unloading-reloading cycle until the octahedral shear strain calculated at the beginning of the cycle is exceeded. When this condition occurs, the material is again in primary loading and the tangent stiffness (in eqs. (1) and (2)) is used as before.

During an unloading phase, a sufficient change in load may actually put the material in tension. In this case, a calculation for modulus that provides a good approximation of the material behavior must be included. Two considerations are appropriate: (1) the soil has little or no strength in tension and (2) a modulus of zero or near zero will create numerical instability. Some assumption must be made that balances these factors to provide a basis for use in computer codes. For this particular model, a modulus equal to one-tenth the initial modulus is used. In addition to this effect, repeated cyclic loading may cause a reduction in strength. To account for this reduction, a cyclic degradation parameter may be used to adjust the stiffness during cyclic loading.

The calculation of constants for the hyperbolic model has been presented in detail elsewhere [8, 12] and will not be presented here. For convenience, tables of typical values for earthfill dams [8] are contained in appendix A. Figure 3 provides an easy calculation sheet for determination of all parameters associated with this model.

### Weidlinger Cap Model

The use of a work-hardening cap as a control on volumetric plastic strain associated with the Drucker-Prager yield surface for the analysis of soils was first suggested by Drucker et al. [6]. A later development, termed the Weidlinger cap model, is used in this report. This model is based on conventional isotropic hardening and the time rate independent plasticity theory with a strain-hardening cap [4, 18]. To simulate nonlinear material behavior such as that illustrated on figure 4, an incremental stress - strain relationship is used. This may be expressed in the rate form as:

$$\frac{d\sigma}{dt} = C^{e-p} \frac{d\epsilon}{dt} \quad (6)$$

where  $C^{e-p}$  is the coefficient matrix for elastic-plastic analysis. Because the material properties are assumed to be time independent,  $dt$  may be eliminated

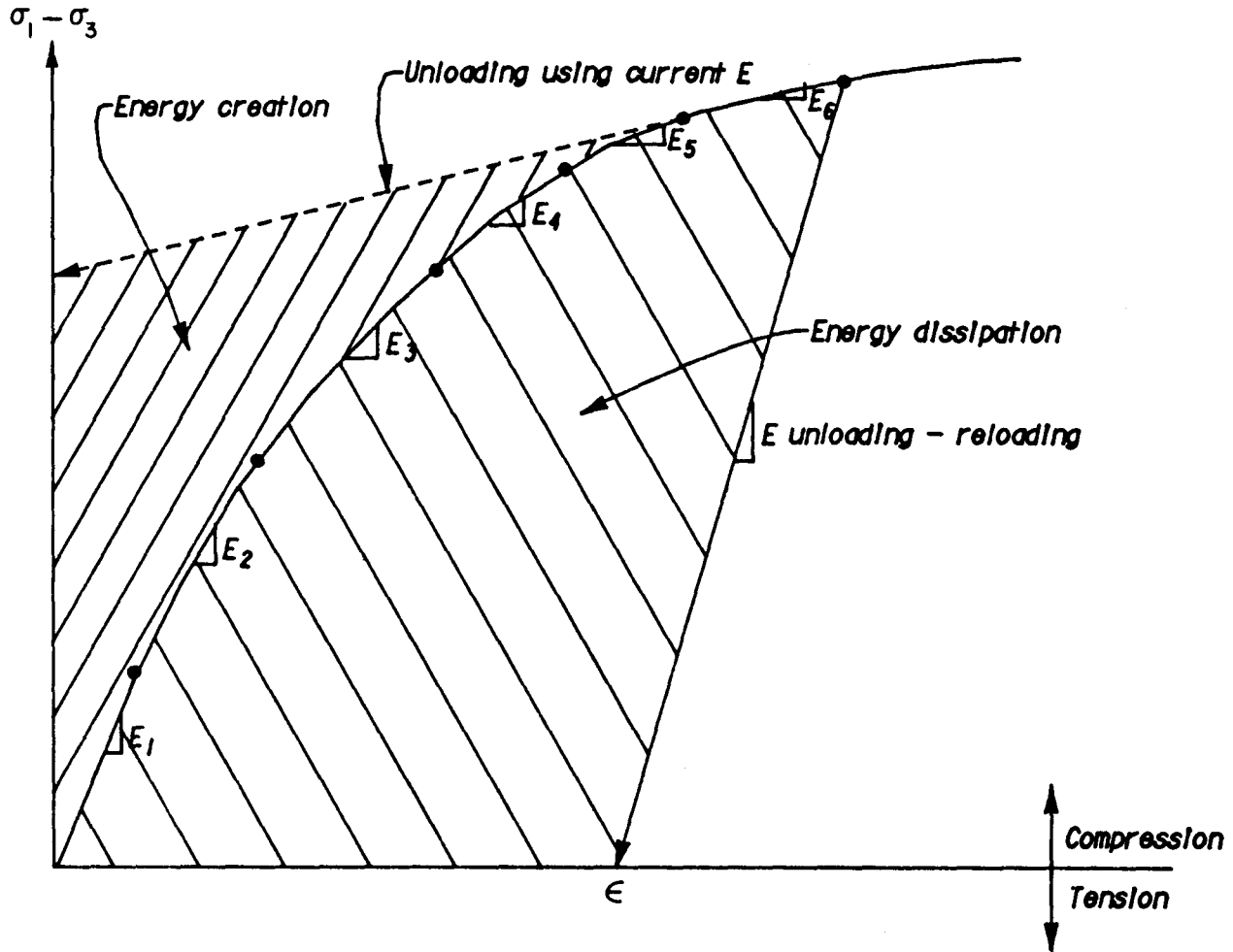


Figure 2. — Example stress-strain curve showing unloading.

or the stress and strain stress rates simply termed  $\sigma$  and  $\epsilon$ , respectively.

The  $C^{e-p}$  component incorporates both elastic and plastic effects. It is derived from the basic concepts of elasticity and plasticity theories by assuming that the strains may be divided into elastic and plastic components, as:

$$d\epsilon_{ij} = d\epsilon_{ij}^e + d\epsilon_{ij}^p \quad (7)$$

where the Cartesian tensor notation is used to imply all components, and the e and p superscripts denote elastic and plastic components, respectively. In addition to consistency conditions, three basic requirements must be satisfied in incremental plastic stress-strain theory:

1. There must be a yield surface. The yield surface is defined as a stress surface which defines plastic yielding and elastic deformations.

Elastic properties are used within the yield surfaces.

2. A flow rule is required. The flow rule relates the relative magnitudes of the strain increments to the stress state. A flow rule for associated plasticity may be achieved by assuming that the yield surface is the plastic potential surface. Plastic strain increment directions are then assumed to be normal to this surface. For the Weidlinger cap model, an associative flow rule is used.
3. A work-hardening law is needed to determine magnitudes of plastic strain increments from a given stress increment.

**Yield Surface.** — The yield surface for the Weidlinger cap model comprises two parts: a stationary failure surface and a strain-hardening cap that reaches from the failure surface to the hydrostatic axis (see fig. 4).

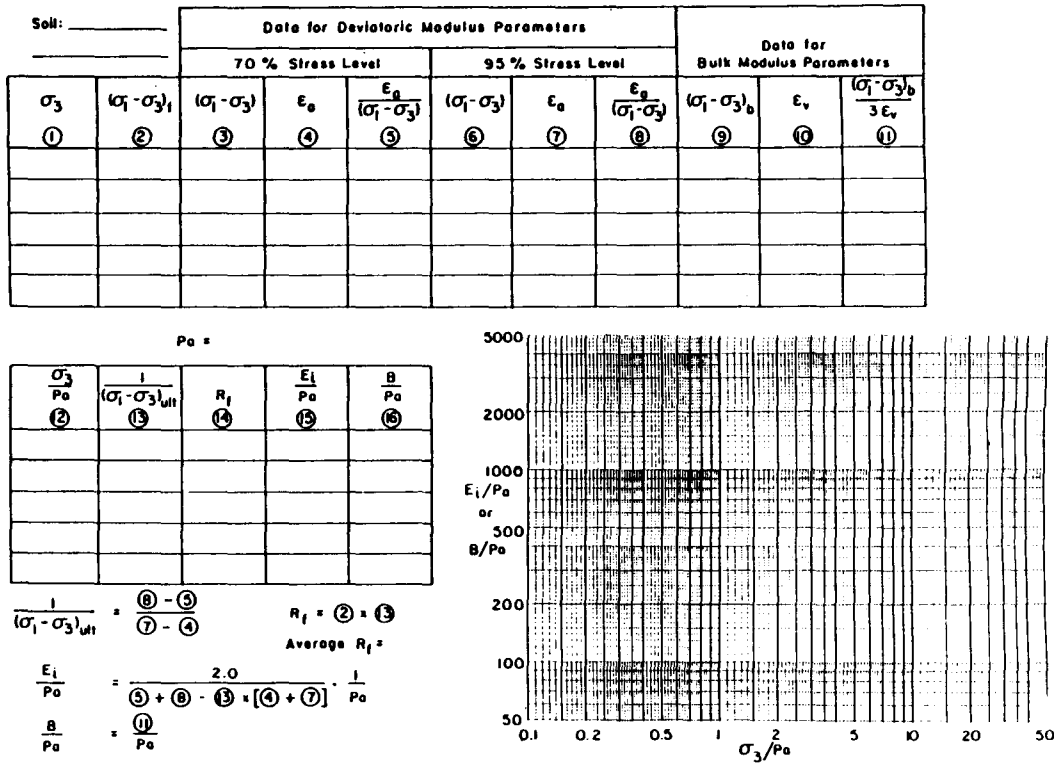


Figure 3. - Calculation sheet for  $E, B$  parameters. From [8].

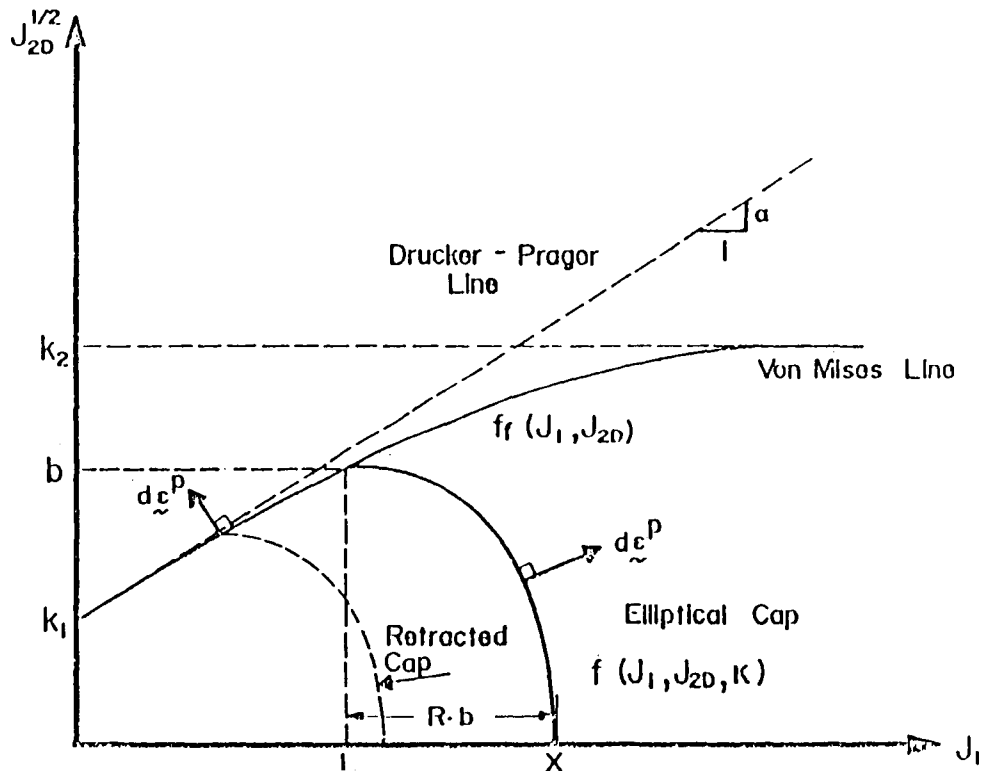


Figure 4. - Ultimate strength and yield surfaces with cap model. From [12].

The upper failure envelope is a composite of the Drucker-Prager surface and a von Mises surface. For lower values of  $J_1$  (the first stress invariant =  $\sigma_1 + \sigma_2 + \sigma_3$ ), the Drucker-Prager criterion is used, or

$$f_f = (J_{2D})^{1/2} - \alpha J_1 - k = 0 \quad (8)$$

where:

$f_f$  = function which expresses yield surface,  
 $J_{2D}$  = second invariant of stress deviator,

$$J_{2D} = \frac{1}{6} [(\sigma_1 - \sigma_2)^2 + (\sigma_2 - \sigma_3)^2 + (\sigma_1 - \sigma_3)^2] \quad (9)$$

where:

$\alpha$  = parameter related to soil friction, and  
 $k$  = parameter related to soil cohesion.

Values of  $\alpha$  and  $k$  must be calculated in conjunction with the boundary assumptions used in the analysis as follows.

For plane strain and matching ultimate stress states with the Mohr-Coulomb strength criterion:

$$\alpha = \frac{\tan \phi}{(9 + 12 \tan^2 \phi)^{1/2}} \quad (10)$$

$$k = \frac{3c}{(9 + 12 \tan^2 \phi)^{1/2}}$$

For axisymmetric conditions:

$\sigma_1 > \sigma_2 = \sigma_3$  (triaxial compression)

$$\alpha = \frac{2 \sin \phi}{3 (3 - \sin \phi)} \quad (11)$$

$$k = \frac{6c \cos \phi}{3 (3 - \sin \phi)}$$

$\sigma_1 = \sigma_2 > \sigma_3$  (triaxial extension)

$$\alpha = \frac{2 \sin \phi}{3 (3 + \sin \phi)} \quad (12)$$

$$k = \frac{6c \cos \phi}{3 (3 + \sin \phi)}$$

As  $J_1$  becomes large, the failure surface is represented by the von Mises surfaces as:

$$f_f = (J_{2D})^{1/2} - k \quad (13)$$

The entire failure surface may be represented by the expression:

$$f_f = (J_{2D})^{1/2} + A - C \exp(-BJ_1) = 0 \quad (14)$$

where  $A$ ,  $B$ , and  $C$  are material constants.

Note that with  $J_1$  equal to zero, equation (8) becomes equation (13) with  $C - A = k$ .

An elliptically shaped moving cap surface is used to complete the ultimate strength surface. This surface has been characterized by two relationships [12]:

$$f_c = \left[ \frac{J_1 - L(S)}{X(S) - L(S)} \right]^2 + \left[ \frac{(J_{2D})^{1/2}}{A - C \exp[-BL(S)]} \right]^2 - 1 = 0 \quad (15)$$

or:

$$f_c = R^2 J_{2D} + J_1 - L(S)^2 - R^2 b^2 = 0 \quad (16)$$

where:

- $S$  = an internal state variable that characterizes the hardening process as a function of the plastic volumetric strain history,
- $L$  = value of  $J_1$  where the elliptical surface intersects the ultimate strength surface,
- $X$  = value of  $J_1$  where the elliptical surface intersects the  $J_1$  axis,
- $R$  = ratio of major and minor axis of the ellipse, and
- $b$  =  $(J_{2D})^{1/2}$  value when  $J_1 = L$ .

Note that  $X$  is the extreme value of  $J_1$  for a given yield surface and corresponds to the isotropic pre-consolidation stress. The isotropic stress states  $X$  and  $L$  are related by the expression:

$$X(K) = L(K) + R [A - C \exp(-BL(K))] \quad (17)$$

**Flow Rule.** — The model is based on an associated flow rule. This assumption requires that during cap action, the plastic strain vector is perpendicular to the cap, or upward and to the right. This implies that the plastic strain rate consists of an irreversible decrease in volume resulting from the irreversible shear strain. Such a volume reduction is intended to model the compaction assumed during compression of most geological materials.

**Hardening Rule.** — The hardening rule used relates the volumetric stress-strain response of the material to isotropic compression. The plastic volumetric strain is assumed to have the form:

$$\varepsilon_v^p = W [\exp(-DX(S)) - 1] \quad (18)$$

where  $D$  and  $W$  are material constants.  $W$  denotes the maximum volumetric plastic strain that can be obtained in isotropic compression relative to the initial conditions. In most applications isotropic compression tests should be conducted to a higher mean stress level than the expected prototype stress level to calculate these parameters. The initial cap position represents the initial preconsolidation stress.

Unloading and reloading are important considerations for the model. Inside the region bounded by the ultimate strength and yield surfaces, all stress paths are treated as elastic, and the initial elastic modulus is used. Thus, any loading sufficient to generate plastic strains increases the elastic region, and all unloadings from the yield line are within the region and treated elastically. Tension conditions follow these same criteria up to a specified tensile limit, beyond which tensile stresses cannot be sustained.

An additional feature that is possible with the cap model is a check for element collapse or excessive increase in volume. These situations arise numerically when elements incur excessive plastic strains. Generally, they cannot occur physically in compression because of the continuity of material, or in tension because of the separation of material and the inability to transfer load to the element. To approximate these conditions, the model monitors plastic volumetric strain. When this parameter exceeds 1.5, elastic properties are used. This allows failure of the material to be initiated, but numerical stability can be maintained to obtain a physically reasonable solution. In cases such as Upper San Fernando Dam (discussed later) this assumption does not allow complete flow of material.

**Evaluating Parameters for the Weidlinger Cap Model.** — To evaluate material constants for the Weidlinger model, at least two tests are needed: a conventional triaxial test and isotropic compression tests. A uniaxial strain test ( $K_o$  test) can be used to improve the accuracy of computed elastic bulk modulus and shear modulus values. A complete description of the calculation of parameters is presented by Ko and Sture [12]. In brief, the constants  $A$ ,  $B$ , and  $C$  represent the configuration of the ultimate strength failure envelope. The  $A$  value is equal to the maximum  $J_{2D}^{1/2}$  value. The constant  $B$  describes the rapidity with which the transition surface approaches the von Mises envelope and can be obtained by trial and error at key points along the surface. When  $J_1 = 0$ , the intercept with the  $J_{2D}^{1/2}$  value is equal to  $C - A$ . The parameters  $D$  and  $W$  are obtained from isotropic compression tests by fitting equation 18 to plastic volumetric strain data.  $W$  denotes a maximum volumetric plastic strain that can be obtained in isotropic

comparison. A ratio between the major to minor axis of the ellipse may be used to find the value of  $R$ . Elastic properties may also be used to approximate the  $R$  value as:

$$R^2 = \frac{9}{G} \left[ \frac{6(1+\nu)}{(1-2\nu)} \right] \quad (19)$$

where:

$$G = \text{modulus of rigidity, and} \\ \nu = \text{Poisson's ratio.}$$

The effect of  $R$  on the strain path is shown on figure 5.

### Pore Pressure Model

The buildup of pore pressure during cyclic loading resulting in reduced effective stress is one of the key components in the reduction of strength in soil materials. By using a model for the pore pressure increase that works in harmony with the stress-strain model, the finite element method is capable of calculating displacements and effective stresses during dynamic loading conditions. In a review of the state-of-the-art for the evaluation of liquefaction potential, Finn [9] discussed several possible approximations to simulate the increase of pore pressure during cyclic loading. In this discussion, the model described relates pore pressure to strain path. Because strains are calculated as variables within the finite element formulation, this model provides a good basis for incorporation in standard stiffness formulated FEM (Finite Element Method) computer codes. Such a relation may be used to find the accumulated pore pressure,  $u_t$ , and thus to calculate the effective stress,  $\sigma'$ , as:

$$u_t = u_o + \Delta u \quad (20)$$

$$\sigma' = \sigma_t - u_t \quad (21)$$

Endochronic models use the concept of intrinsic time to relate independent and dependent variables of the response to suitable transformed variables [9]. The functions generated are a single monotonically increasing function. Sand at a given relative density, subjected to cyclic loading tests, can be represented by single pore pressure functions over the ranges of stresses or strains of usual interest. In the case where a single function is not satisfactory, a piecewise fit may be constructed treating various ranges of strains over the entire interval. The use of a single function provides a conceptually straightforward implementation into finite element analyses.

Consider a simple cyclic shear test as shown on figure 6. A sample is loaded vertically by a stress  $\sigma_v$ .

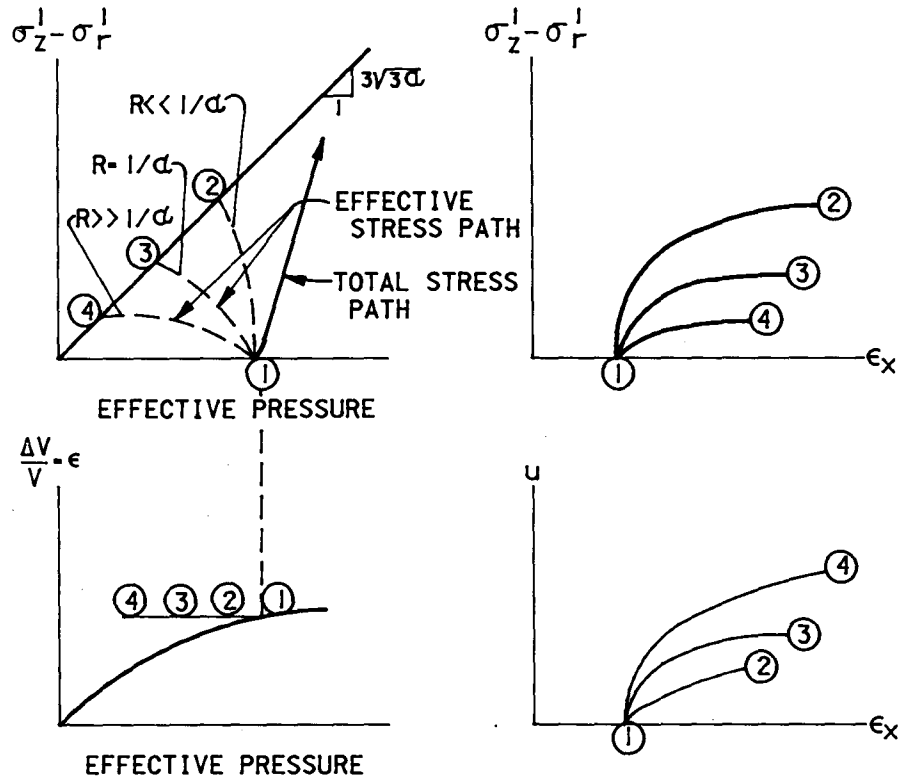


Figure 5. - Effect of soil parameter  $R$  on undrained strain path. From [1].

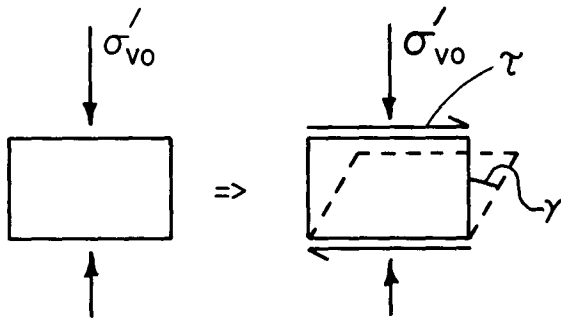


Figure 6. - Simple cyclic shear strain test.

and subjected to a shear stress  $\tau$  applied in a cyclic loading process.

Typical experimental data using this test are shown on figure 7. It is clear from figure 7 that the pore pressure ratio is a function of the shear strain amplitude in the test and the number of cycles.

The development of pore pressure may be related to the total strain history instead of the number of cycles by summing incremental shear strains at each step of the calculation. An incremental strain path parameter,  $d\xi$ , is chosen as:

$$d\xi = (de_{ij} de_{ij})^{1/2} \quad (22)$$

where  $e_{ij}$  is the deviatoric total strain tensor. For the simple shear test,  $d\xi$  may be expressed as:

$$d\xi = dy/2 \quad (23)$$

where  $\gamma$  = the amplitude of the shear strain. The strain path parameter,  $\xi$ , is a monotonically increasing parameter to track the number of cycles, strain history, etc. The data on figure 7 are plotted on figure 8 in terms of strain path length,  $\zeta$ .

To map all curves of constant strain data to a single curve, a suitable transformation variable,  $T$ , is required. Finn [9] suggests the function:

$$T = \exp(\lambda\gamma) \quad (24)$$

where  $\lambda$  equals a pore pressure constant which is a function of the material under consideration. By using this transformation parameter, the test values are transformed to a new single parameter,  $\kappa$ , referred to as the damage parameter, or:

$$\kappa = \zeta[\exp(\lambda\gamma)] \quad (25)$$

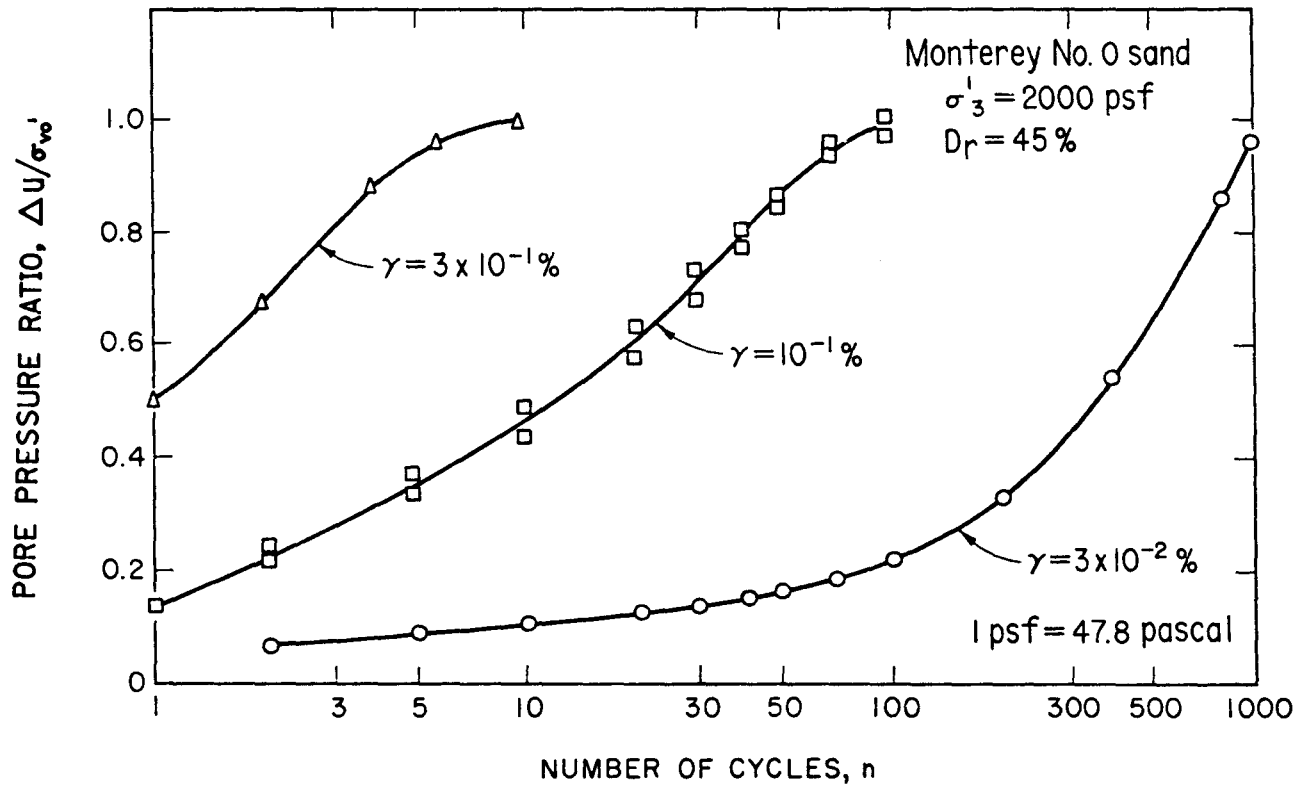


Figure 7. - Plot of typical cyclic strain data. From [5].

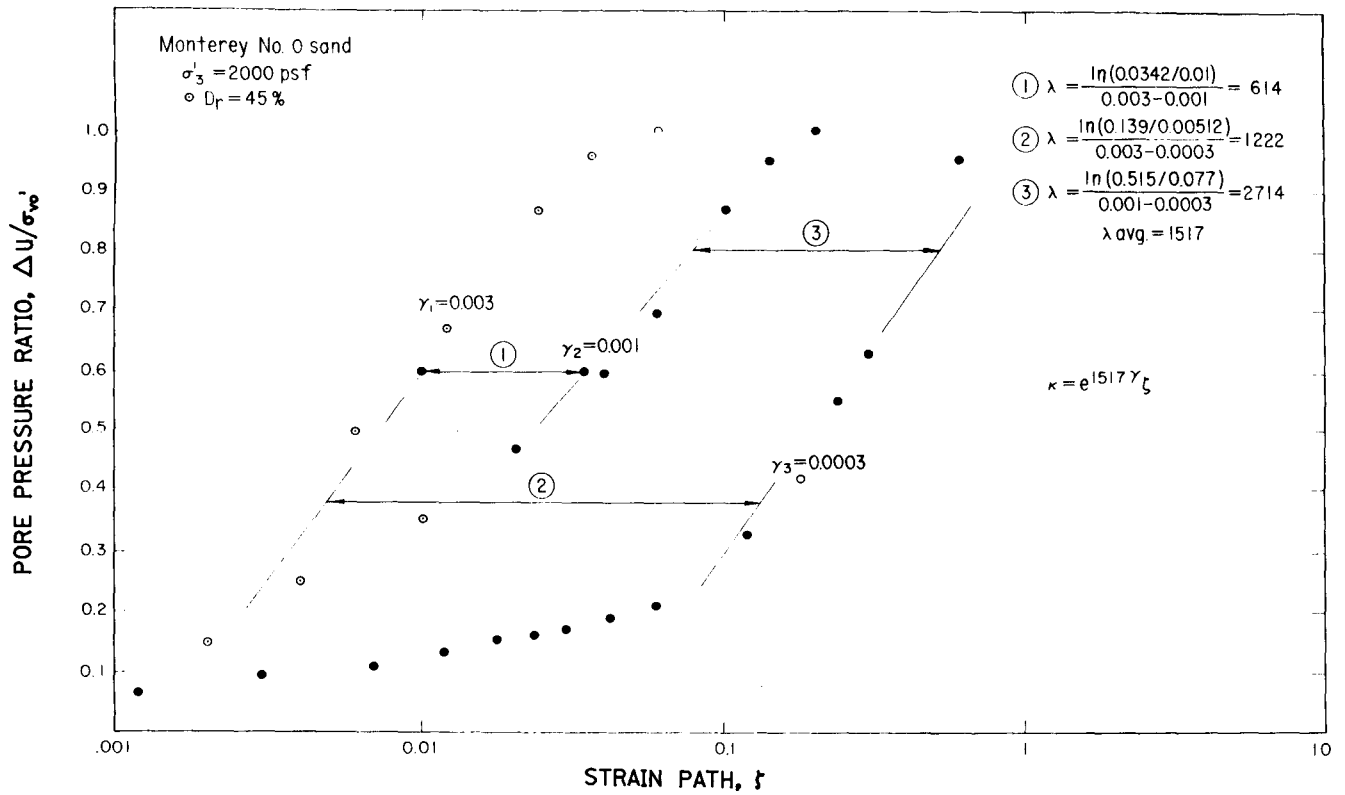


Figure 8. - Plot of  $\Delta u/\sigma'_{v0}$  vs.  $\zeta$  for cyclic strain data.

Plots of the damage parameter and pore pressure normalized by the initial confining stress can be generated from test data (see fig. 9). The range of values are plotted on a semi logarithmic scale. A general equation was used to match the data in this form [9], and it was found that the best linearization was made by the use of the equation:

$$\frac{u}{\sigma_{vo}'} = \left(\frac{A_u}{B_u}\right) \ln(1 + B_u \kappa) \quad (26)$$

where  $\sigma_{vo}'$  equals initial confining pressure of the test, and  $A_u$  and  $B_u$  are constants determined for each soil.

Similar relationships may be used for triaxial test conditions to produce a single expression for pore pressure. For this case, the strain path parameter,  $\zeta$ , may be expressed in terms of stress [9] as:

$$d\zeta = (d\sigma_{ij} d\sigma_{ij})^{1/2} \quad (27)$$

and the strain damage parameter may be defined as:

$$\kappa = \zeta [\exp(\lambda \frac{\sigma_d}{2})] \quad (28)$$

where  $\sigma_d$  equals cyclic deviator stress. Pore pressure is calculated using equation 26 as before.

**Determination of Material Constants.** — Typical cyclic strain data are shown on figure 7. Three different shear strain values are shown for the tests:  $\gamma = 0.003$ ,  $\gamma = 0.01$ , and  $\gamma = 0.0003$ . The data may be plotted as  $\Delta u/\sigma_{vo}'$  versus  $\zeta$ , as shown on figure 8. With data in this form, the pore pressure constant,  $\lambda$ , may be calculated by interpolating values of change in  $\zeta$  for different strains at a constant pore pressure (see fig. 8). Since the constant,  $\lambda$ , is used to interpolate different ranges of strain to the single variable,  $\kappa$ , the derivation of  $\lambda$  may be accomplished for two levels of strain amplitudes,  $\gamma_1$  and  $\gamma_2$  as:

$$\kappa = \zeta_1 \exp(\lambda \gamma_1) = \zeta_2 \exp(\lambda \gamma_2) \quad (29)$$

Rearranging the expression and solving for  $\lambda$ , we obtain:

$$\exp[\lambda(\gamma_1 - \gamma_2)] = \zeta_1/\zeta_2 \quad (30)$$

or

$$\lambda = \ln \frac{(\zeta_2/\zeta_1)}{(\gamma_1 - \gamma_2)} \quad (31)$$

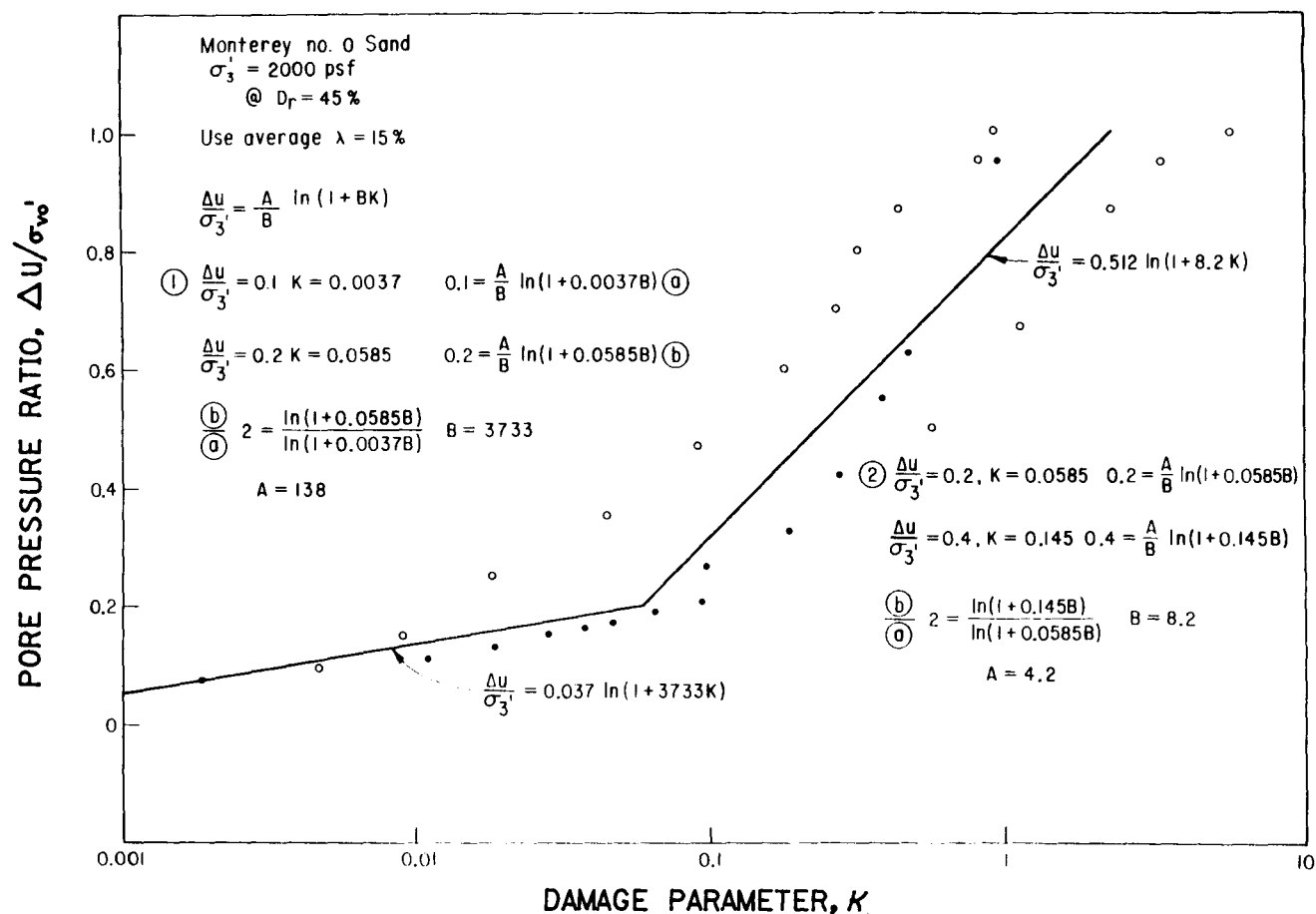


Figure 9. — Plot of  $\Delta u/\sigma_{vo}'$  vs.  $\kappa$  for cyclic strain data ( $\lambda = \text{constant}$ ).

as shown on figure 9; an average or weighted average may be necessary. For this example, the calculation of the strain path (fig. 8) may be represented by:

$$\kappa = \exp(1517\gamma\zeta) \quad (32)$$

The constants  $A_u$  and  $B_u$  remain to be found. A new graph may be produced using equation 26 to transform the data to a form that may facilitate formulation of a single function. Figure 9 shows this transformation. As can be seen in the graph, the best fit for the data is two straight lines, and an average value is introduced as shown on the figure. Alternatively, the transformation may be carried out by using different values of  $\lambda$  for different stress ranges. The best bilinear fit using this method is on figure 10, and it can be seen on the figure that this fit is significantly better. It is this method of varying values of  $\lambda$  and constants  $A_u$  and  $B_u$  for ranges of  $\kappa$  that is implemented in this work.

For triaxial experimental data, a similar procedure can be adopted. Typical data, which were developed by the Bureau's Soils Testing Section in 1981 [3], are shown in tables 1 through 5. In these tables, note that the axial strain in percent is tabulated from the

test data. To calculate shear strain for undrained conditions, the relationship used is:

$$\gamma_{max} = \frac{3}{2} \varepsilon_a \quad (33)$$

where  $\varepsilon_a$  equals axial strain. Should this be an inappropriate assumption, another relationship of axial strain to shear strain must be devised. The strain path,  $\zeta$ , is then calculated as twice the shear strain (1 cycle) accumulated for each cycle. The values may be plotted to find values of the transformation parameter,  $\lambda$ . In this case, a single value is calculated from:

$$\lambda = \frac{\ln(\zeta_2/\zeta_1)}{\gamma_1 - \gamma_2} \quad (34)$$

$$\begin{aligned} \text{for: } \gamma_1 &= 0.16, \zeta_1 = 0.50, \text{ and} \\ \text{for: } \gamma_2 &= 0.20, \zeta_2 = 0.185 \end{aligned} \quad (35)$$

Therefore:

$$\lambda = \frac{\ln(0.185/0.50)}{0.16 - 0.20} = 24.86 \quad (36)$$

The remaining calculations for  $A_u$  and  $B_u$  are identical to that displayed for the cyclic strain data shown on figures 9 and 10. They are shown for this example on figures 11 and 12.

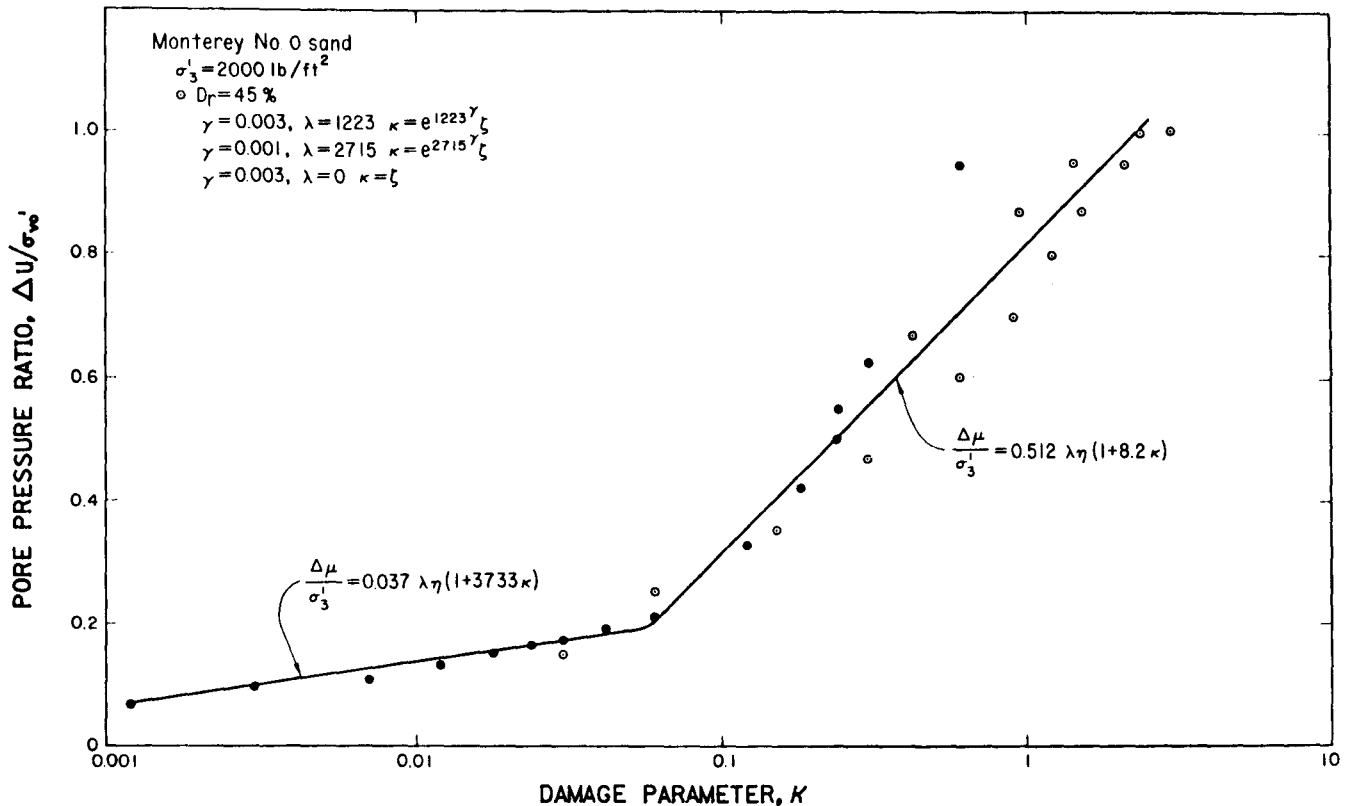


Figure 10. - Plot of  $\Delta u/\sigma'_{v0}$  vs.  $\kappa$  for cyclic strain data ( $\lambda = \text{variable}$ ).

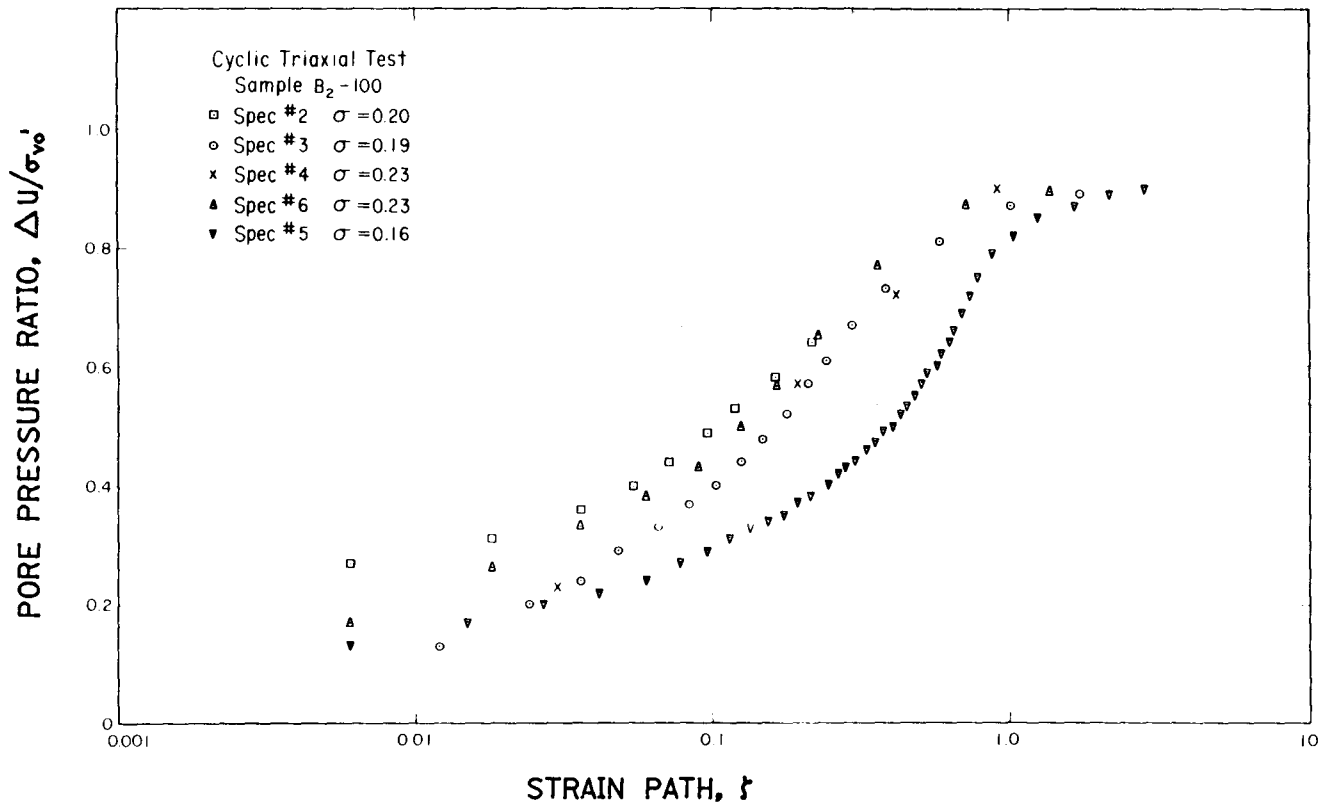


Figure 11. — Plot of  $\Delta u/\sigma'_{v0}$  vs.  $\zeta$  for cyclic triaxial data.

## CYCLIC TRIAXIAL TEST PREDICTION

To test the implemented models, a comparison with a triaxial test was made. Data for this test were obtained at the Bureau laboratory, using 2-inch-diameter samples subjected to 10 hertz. To simulate the triaxial test, an axisymmetric finite element mesh was used as shown on figure 13. The confining pressure was first applied in a loading sequence, then axial loads were applied. The results plotted for elements 63 or 64 and node 88 (unless otherwise noted) are assumed to represent typical results.

Results for the hyperbolic model are shown on figure 14. Note the ability of the hyperbolic model to model the elbow in the displacements curve. This shows the ability of the cyclic degradation parameter, discussed previously, to model the loss of strength in the material. This was accomplished by degrading the strength 10 percent in each load cycle, as was observed in the lab data.

Figure 15 shows the use of the cap model and the endochronic pore pressure model to simulate the same cyclic triaxial test. In this case, element 55 (an edge element) closely models the pore pressure while element 63 (a central element) produces an underprediction of approximately 20 percent at the

higher pore pressures. Note that the measurements taken during the test are at the edge of the specimen or in a location similar to that of element 55. This model shows contours of pore pressures that are greater and that approach liquefaction near the ends and less in the interior. The model results certainly show the correct pattern of an onset of pore pressure for both elements. Quantitatively, these results are reasonably close to the actual results. The displacements modeled do not show an elbow as the hyperbolic model did, but they do provide an approximate representation of the displacements.

## DAMS SUBJECTED TO EARTHQUAKES

### Oroville Dam

Oroville Dam is an embankment structure on the western slope of the Sierra Nevada, approximately 85 miles north of Sacramento, California. It is 770 feet high and 5,600 feet long between abutments. The maximum cross section is shown on figure 16. Zoning in the dam consists of an impervious core, gravel shells, and transition zones. Materials in the shells were obtained from extensive fields of tailings remaining from gold mining operations. The dam was completed in 1967, after a 5-year construction period.

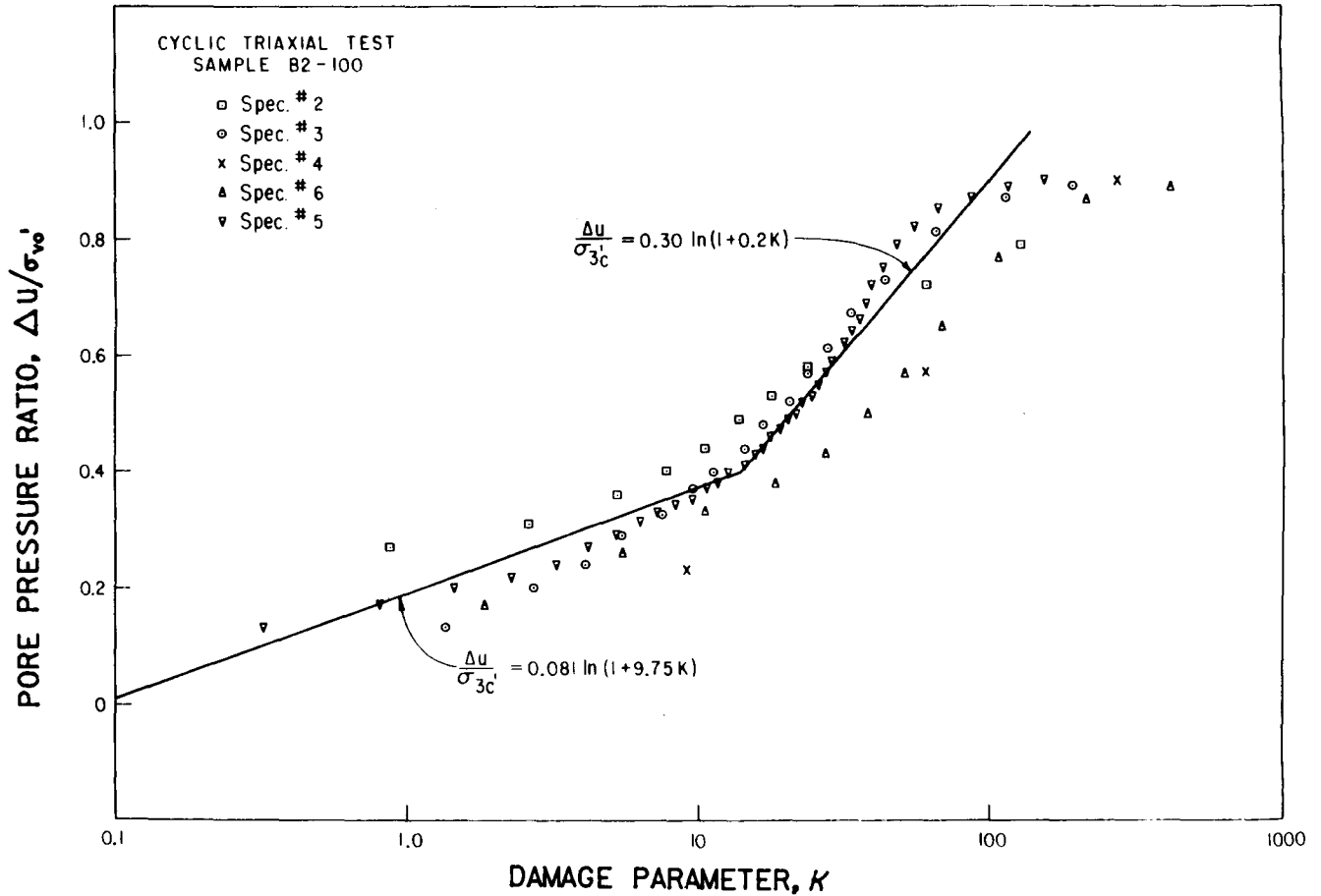


Figure 12. - Plot of  $\Delta u/\sigma'_{v0}$  vs.  $K$  for cyclic triaxial data.

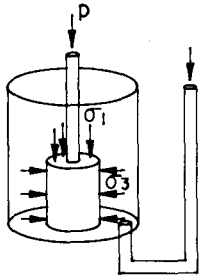
Construction of the dam was done directly on a very hard and sound amphibolite rock. Foundation movements were small compared with movements in the dam throughout the construction period [14].

At the time of the earthquake, the water elevation in the reservoir was 900 feet. No seepage problems were reported before the event. The dam was instrumented extensively, and normal seepage and movements were observed for the dam up to the time of the earthquake.

The major earthquake pulse, which occurred on August 1, 1975, had a 5.7 magnitude. Instruments on the dam were triggered and the acceleration history was recorded. Unfortunately, because of a power failure, part of the record was lost. The missing portions of the earthquake record were replaced by using acceleration records from subsequent quakes, which in turn were readjusted to conform to the given magnitude. The entire history is shown on figure 16. Displacements, which were measured by instruments in the dam during the earthquake, were quite small.

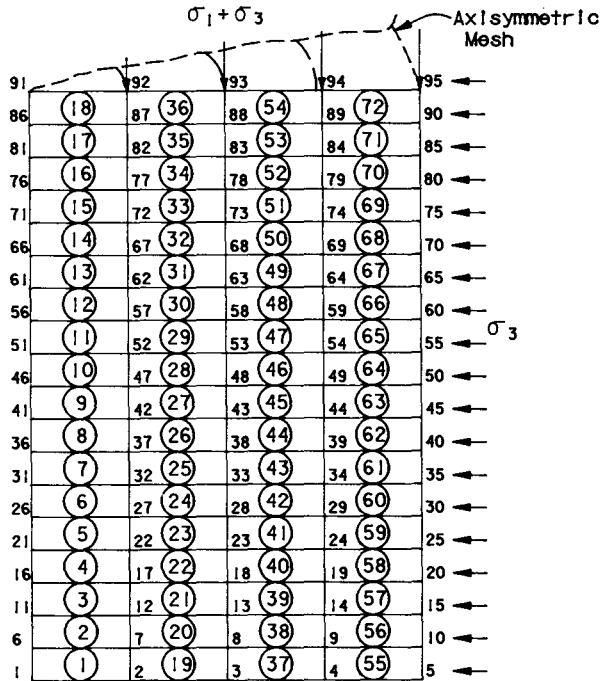
Properties used in each model are presented in table 6. Hyperbolic properties were selected for materials that were most closely related to Oroville materials based on the description by Duncan et al. [8]. Parameters for the cap model were not available but were calculated or chosen from published literature. This process for determining the cap model parameters for Oroville Dam is contained in appendix B. Note that for displacements this small, a linear elastic material model would undoubtedly have produced good results. Thus, the ability of the described material models to predict nearly elastic behavior is verified by this case.

An analysis was done to simulate gravity loads in the mesh in a single step. Previous analyses by Kulhawy and Duncan [14] suggested the use of construction layers to best simulate the gravity effects in the dam. A comparison of results for chosen elements (circled stress values) and the previous analysis are shown on figure 17. It can be seen from this figure that the stress results are closely approximated, thus producing the correct in situ conditions to be used before the occurrence of the earthquake. Note that this also



① Elements  
i Node

TRIAXIAL TEST



CYCLIC TRIAXIAL TEST IDEALIZATION

Figure 13. - Cyclic triaxial test idealization.

implies that no significant nonlinear behavior has occurred under this loading from large displacements or from the stress path.

In all of the finite element analyses, accelerations are applied in the base of the mesh, and the Newmark method is used to calculate accelerations throughout the mesh. Points from time steps of 0.1 second from the Oroville analysis are plotted on the actual measured crest accelerations on figure 18. It can be seen from this plot that accelerations of appropriate sign, magnitude, and period are calculated. Hysteretic effects of loading and unloading are approximated by the numerical material model. Stiffening or loss of stiffness are correctly approximated with this analysis to match the measured and predicted results.

The displacements predicted for the Oroville Dam case are nearly 1 inch of movement for static and

dynamic effects. In the actual field case, the dam reacted to the earthquake loads elastically (or showed no permanent displacement). The analysis can be considered to be elastic with deflections of this magnitude. Likewise, the cap model predicts nonfailure for this case under dynamic loading. The displacements of the model show distortions of less than 2 feet, which are greater than those imposed in the field loading. However, this was primarily caused by the crudeness of the selection of material model parameters. Thus, it can be seen that the predictions are essentially the same as the available measured parameters for the dam.

### Sheffield Dam

The Sheffield Dam was an embankment dam, 720 feet long and 25 feet high, located in a ravine north of Santa Barbara, California. A representative section of its maximum cross section is shown on figure 19 [21]. Construction of the dam was completed during the winter of 1917.

Material for the dam was excavated from the reservoir and compacted by the movement of the construction equipment. The main portion of the dam was composed of a mixture of silty sand and sandy silt containing some cobbles and boulders. On the upstream face, a 4-foot-thick blanket of clay that extended 10 feet into the foundation was constructed. A 5-inch concrete facing was placed over the clay blanket.

The foundation is a terrace alluvium 4 to 10 feet thick overlying sandstone bedrock. Drilling done by the Corps of Engineers revealed a silty sand and sandy silt soil containing some material 3 to 6 inches in diameter. Some thin layers of clayey sand and generally sandy clay were found. The upper 1 to 1.5 feet of foundation soil were found to be slightly looser than the deeper material.

At the time of the earthquake, the depth of the reservoir was 15 to 18 feet. Seepage had been noted at the toe of the downstream slope before the earthquake. Inspectors of the dam believed that the foundation of the dam had become saturated by percolation. The assumed water level is shown on figure 19 [21].

The main shock of the Santa Barbara earthquake occurred at 6:42 a.m. on June 29, 1925. No recorders for motions existed at that time. However, on the basis of records at distant stations, the earthquake was assigned a magnitude rating of 6.3, with an epicenter located 7 miles northwest of the damsite. To obtain a representative accelerogram for this site, the 1940 El Centro earthquake was selected [21] because it occurred at a similar epicentral recording distance as the Santa Barbara quake. The El Centro

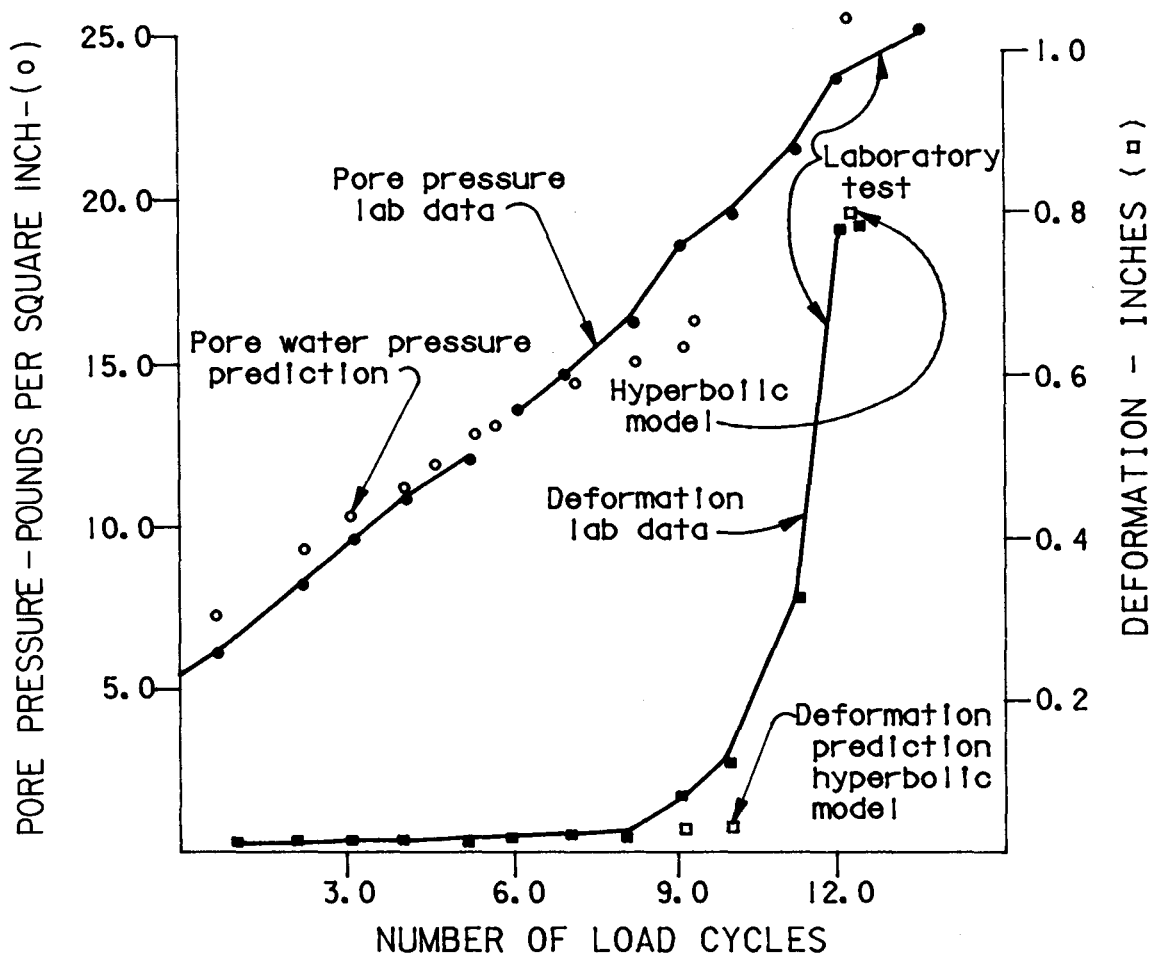


Figure 14. - Hyperbolic cyclic triaxial results. Laboratory test results from [3].

earthquake record was scaled for ordinate values of 0.15 g and abscissa values showing a predominant frequency of 3 cycles/s continuing for 15 seconds, as shown on figure 19.

The failure of the embankment was reported as "a great mass of the center," about 300 feet in length, sliding downstream about 100 feet. It is assumed that the sliding occurred on a surface near the base of the embankment [21]. The sliding was related to a severe reduction in soil strength and resulting increases in pore water pressure induced by the earthquake loading.

The material properties for Sheffield Dam were selected using methods similar to those discussed for Oroville Dam. They are listed in table 7. No properties were available for liquefaction simulation using the endochronic model, so the values calculated for the San Fernando dams were used.

To correctly model the Sheffield case history, a complete failure had to be predicted. The displacement configurations calculated by the hyperbolic model at

various time steps during the first second of earthquake loading are shown on figures 20, 21, and 22. Note that the displacements are shown at the same scale as the dam geometry. In these figures it can be seen how the mesh must deform to model a complete failure. On figure 21, a definite toe failure appears (at time 0.530 second). By time 0.630 second (fig. 22), complete downstream movement has begun throughout the dam.

Displacement vectors are shown on figure 23 for the displaced mesh on figure 22 at time 0.630 second. The toe bulging is evident from the displacement vectors on the downstream slope of the dam. High shear zones, or shear surfaces, are bounded by arrows in opposite directions. One such zone is shown near the bottom of the dam exiting low on the upstream face. This location is consistent with observations after the failure of the dam. A small vertical movement is shown under the crest of the dam. This zone exists because of the change in direction of motion between the upstream and downstream portions of the dam, i.e. down and downstream on the left side of the dam, and down and upstream on the right side

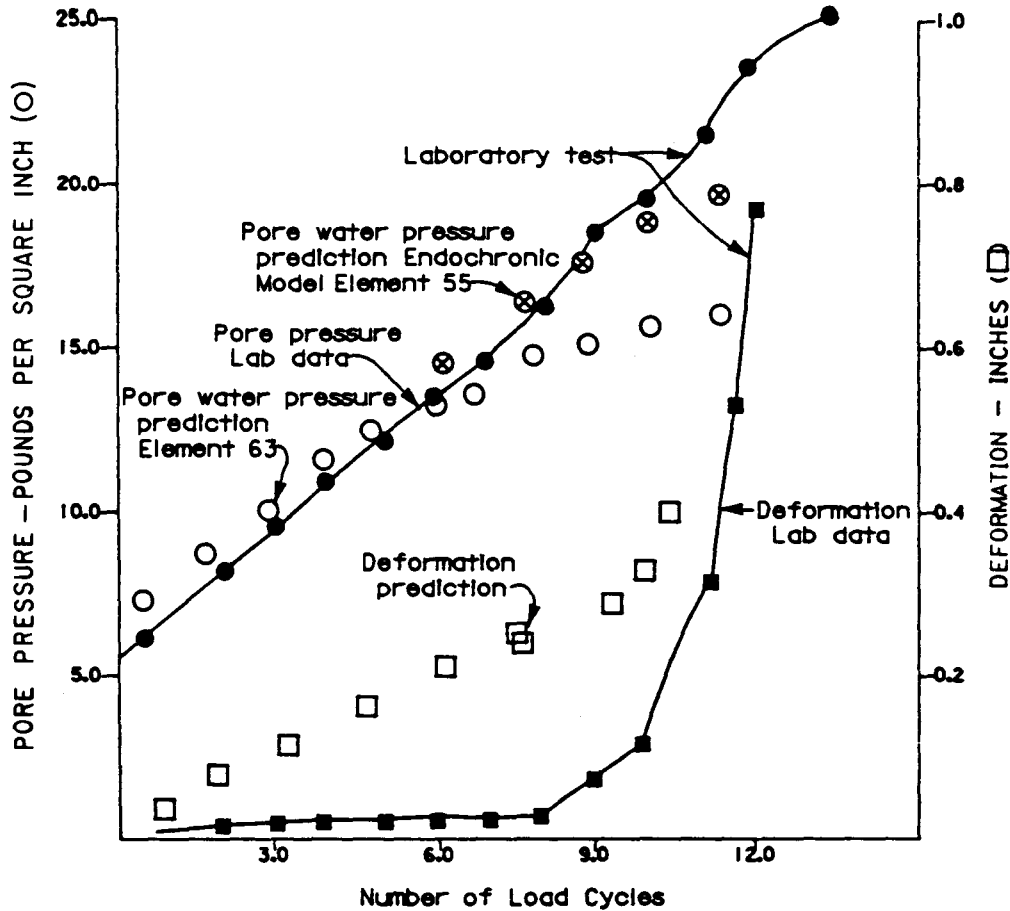


Figure 15. - Cap model cyclic triaxial results. Laboratory test results from [3].

of the dam. Displacements of the failed dam cannot be predicted using the small deformation theory. Geometric nonlinearities would improve the analysis, but would require more costly and elaborate computer methods. The prediction definitely shows a complete downstream failure as occurred in the field, but it cannot calculate the final position of the dam at the end of the earthquake. Note, however, that in support of design or in safety evaluations, the final position is inconsequential, only the fact that the dam will fail is important.

The failure of the dam is predicted at time 1.003 seconds or after 200 time steps. Exactly when the dam actually failed during the earthquake is not known, but it is unlikely that failure occurred as rapidly as predicted here. Pore pressure parameters taken from the San Fernando dams are probably too large, thus producing an onset of liquefaction too quickly. Dissipation of pore pressure caused by dilation is not used in the pore pressure model, and thus buildup and dispersion of zones of liquefied material require longer earthquake loading in the actual case to produce a failure. However, as mentioned before, the time of failure is not as important in support of design as the fact that the failure will occur.

As will be shown in the Upper San Fernando Dam case presented later, failures are not predicted for all cases.

Of additional interest is how the onset of liquefaction occurs. The mesh for Sheffield Dam contains only one layer of liquefiable elements; therefore, this case is easy to study. Figure 24 shows the progression of liquefaction as a function of time step through the mesh. Note on the figure that elements under approximately one-half the height of the dam liquefy first, and the zone becomes larger toward the edges of the dam as the earthquake loading continues. This means that zones subjected to the highest load, and thus the highest strain, liquefy first.

Cap model results also predict complete failure of the dam. On figure 25 (time 0.405 second), it can be seen that a toe bulge failure and a disruption under the concrete blanket has occurred. This is completely consistent with the failure surface present after the earthquake. Note also the failure in the foundation, which was the area suspected of resulting in ultimate failure. Figure 26 (time 0.430 second), shows a complete failure of this region. At later times, a complete displacement of the downstream portion of the dam

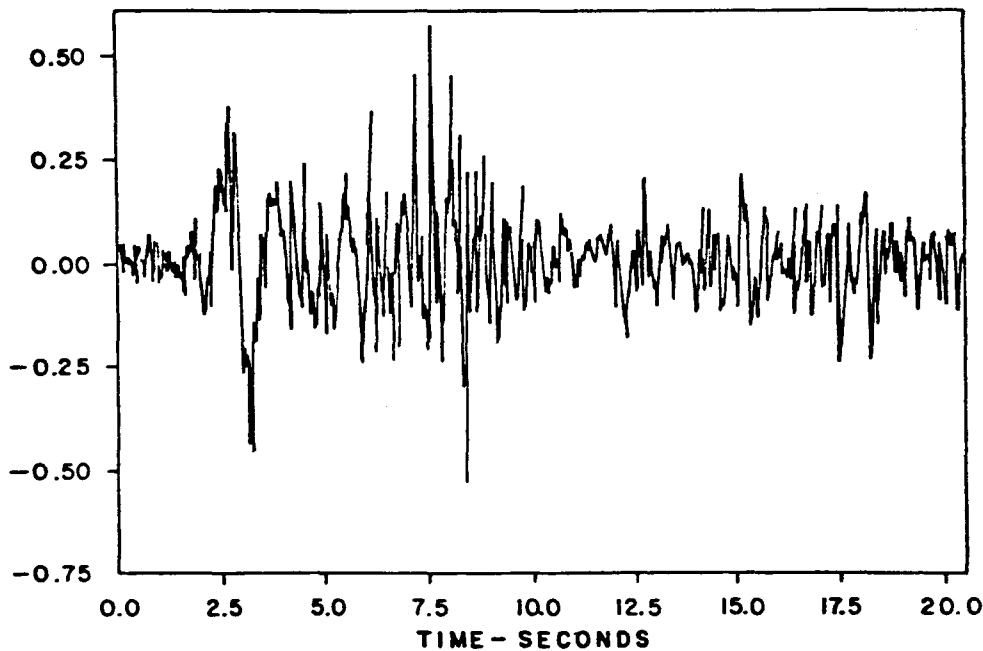
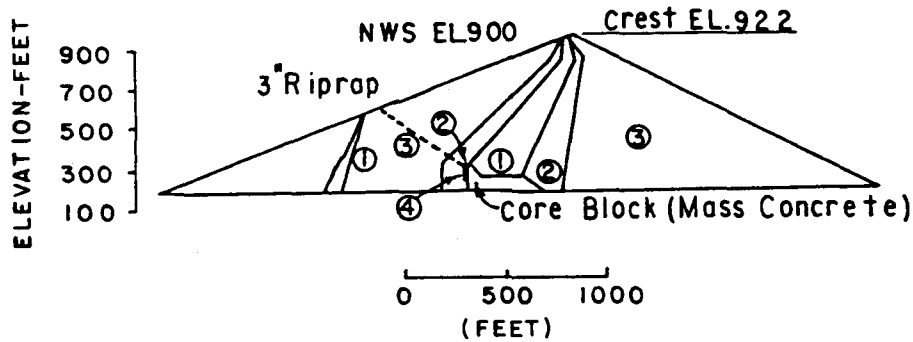


Figure 16. - Maximum cross section and earthquake record of Oroville Dam. From [14].

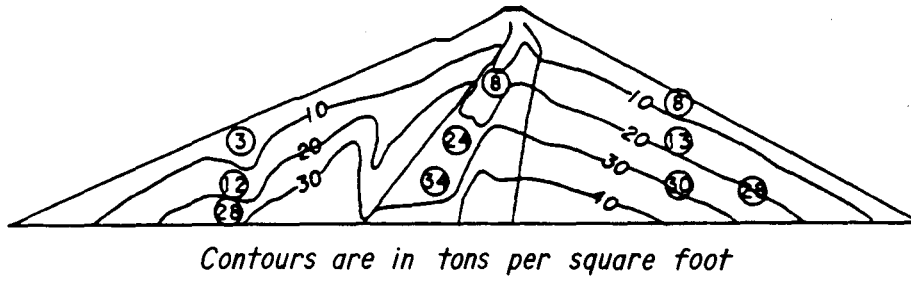
occurs. Note how there is only small disruption in areas away from major failure regions. This is consistent with the belief that a slip surface occurred through the foundation. A complete failure which, of course, occurred is predicted for the time 0.430 second after the beginning of the earthquake. This time is probably incorrect, as discussed before concerning the hyperbolic model. The prediction of failure is, however, correct.

Displacement vectors are shown on figure 27 for the distorted mesh on figure 26 (time 0.430 second). A failure mode showing the division of the dam into two distinct regions is observed. The upstream portion of the dam is sliding upstream, and the down-

stream portion of the dam is sliding downstream. Under this failure mode, the dam would flatten and not necessarily slide downstream as observed in the field. Note, however, that the predominant vectors are downstream. Assuming this continues, portions of the upstream slope would also slide, thus following more closely the observed failure mechanism.

#### Lower San Fernando Dam

Lower San Fernando Dam was an embankment dam, 2,080 feet long and 142 feet high at the maximum section. A representative section of the maximum cross section is shown on figure 28 [22]. The construction began in 1912 when hydraulic fill methods



○ *Computed this study*  
 — *Contours from reference*

Figure 17. — Comparison of stress results using construction layers and gravity turn on. From [14].

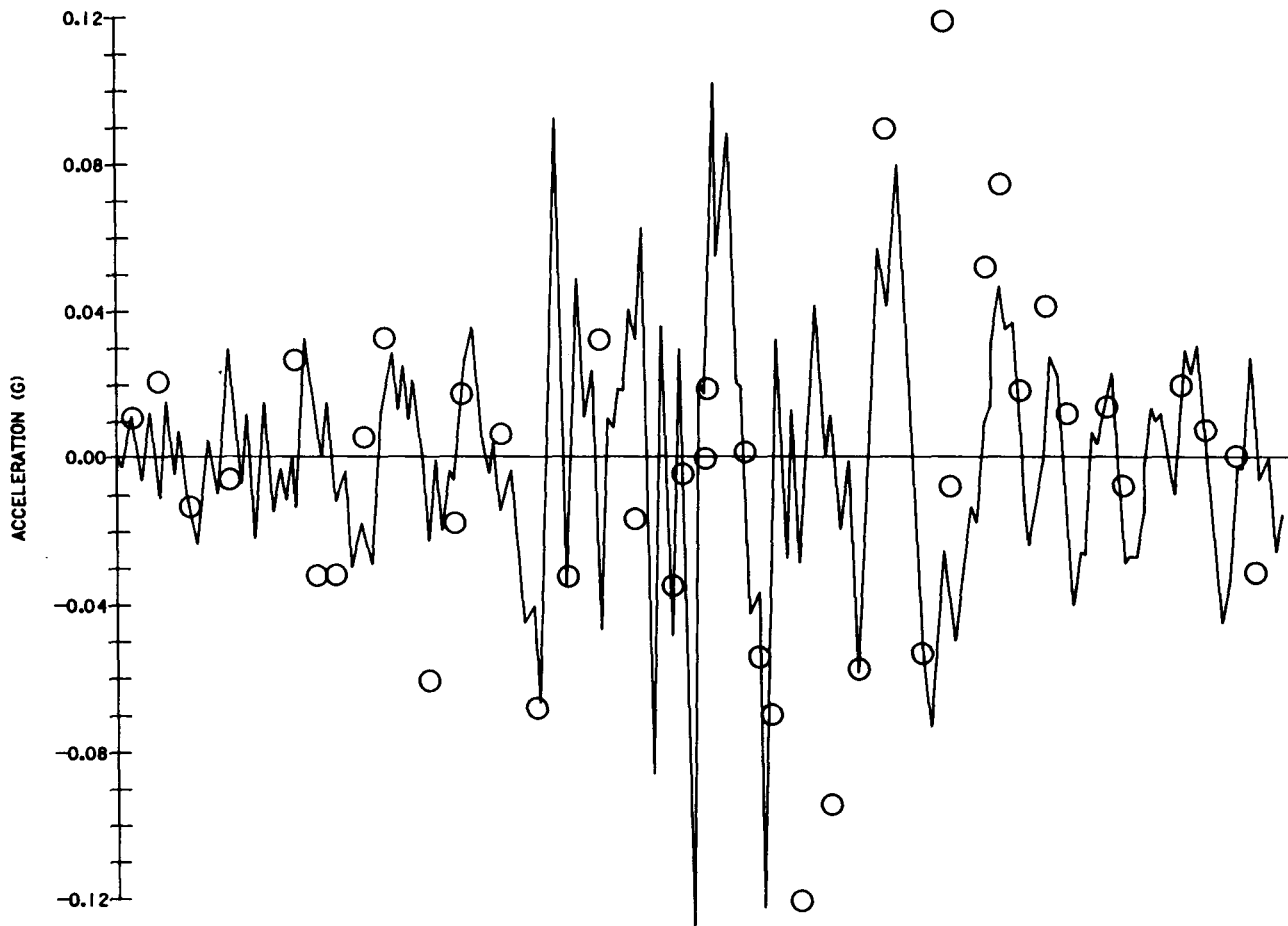


Figure 18. — Comparison of computed and measured crest accelerations. From [23].

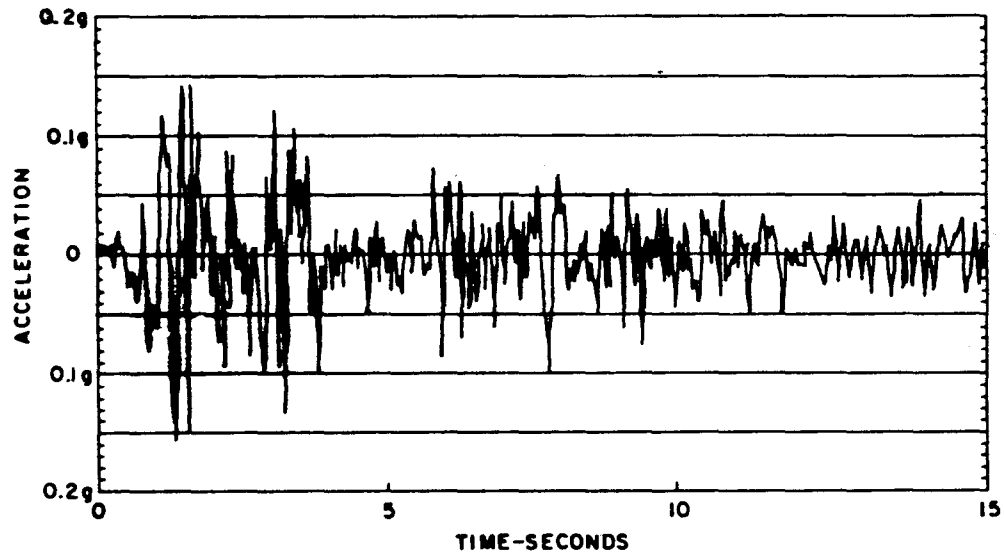
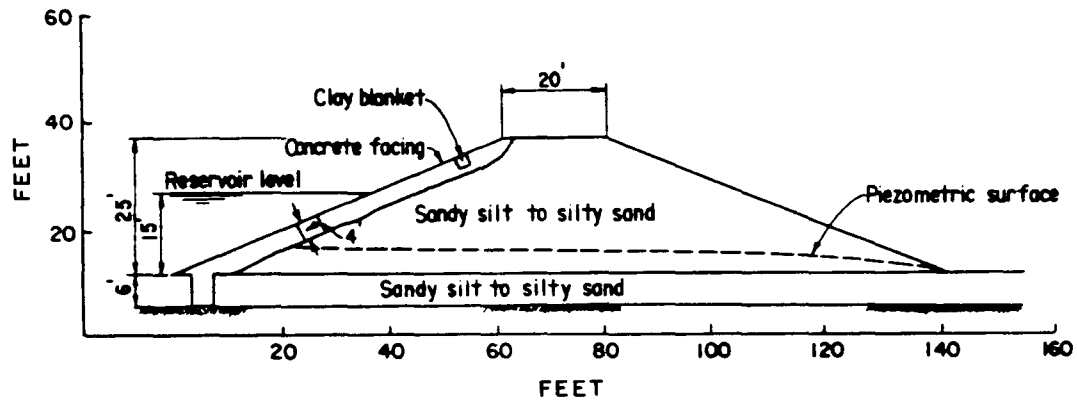


Figure 19. – Cross section and earthquake record of Sheffield Dam.  
From [21].

were used for approximately the first 100 feet of elevation. The dam was raised several times and construction continued through 1930. In 1915, ground-up shale was used for approximately 7 feet of fill. This section was then capped by a layer of rolled fill. The dam was raised in 1920, 1924, and 1929-30, by adding fill to the dam. In 1940, a rolled-earth berm was added downstream.

The foundation for the channel section of the dam and for lower portions of the abutments consists of recent alluvium made up of stiff clay with lenses of sand and gravel. Beneath the dam, a maximum thickness of 35 feet of this material exists. Below this alluvium and in the upper elevations of the abutment

are shales, siltstones, and sandstones. The upper 30 to 50 feet of the left abutment shales and siltstones are weathered to varying degrees and contain numerous gypsum-filled seams along joints and bedding planes. The right abutment is underlain by a massive deposit of friable sandstone.

At the time of the earthquake in 1971, the elevation of the reservoir was 1110 feet, or 115 feet of head. Excessive seepage had been a problem in the left abutment until extensive grouting was completed in 1964.

At 6:00 a.m. on February 9, 1971, an earthquake of 6.6 Richter magnitude occurred. The epicenter of the

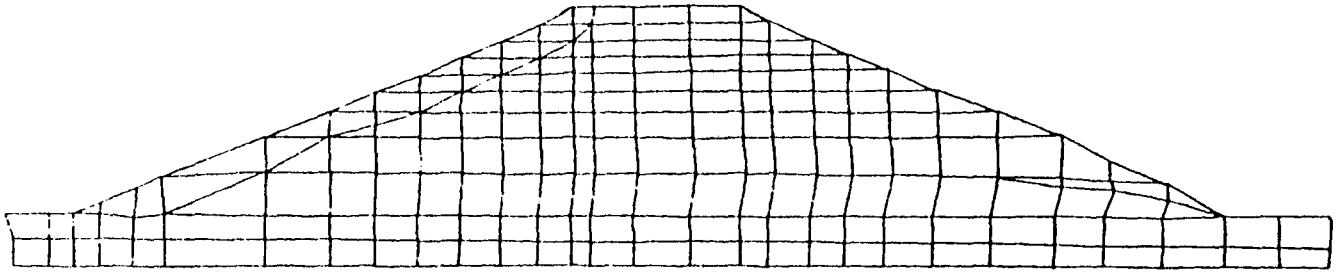


Figure 20. – Hyperbolic prediction for time 0.505 second – Sheffield Dam.

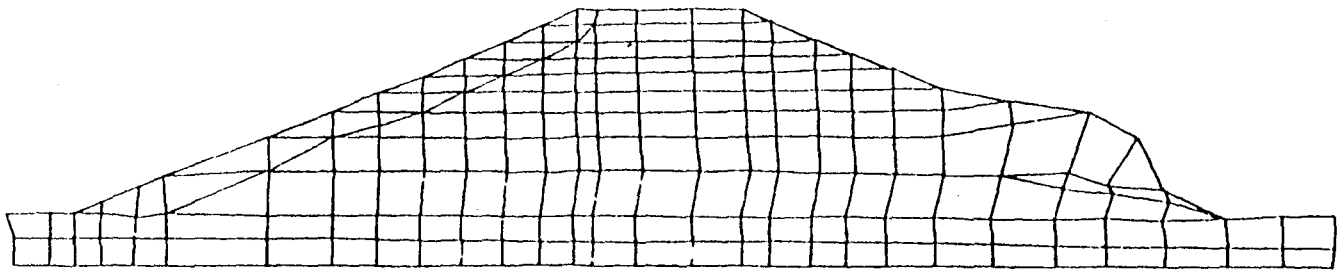


Figure 21. – Hyperbolic prediction for time 0.530 second – Sheffield Dam.

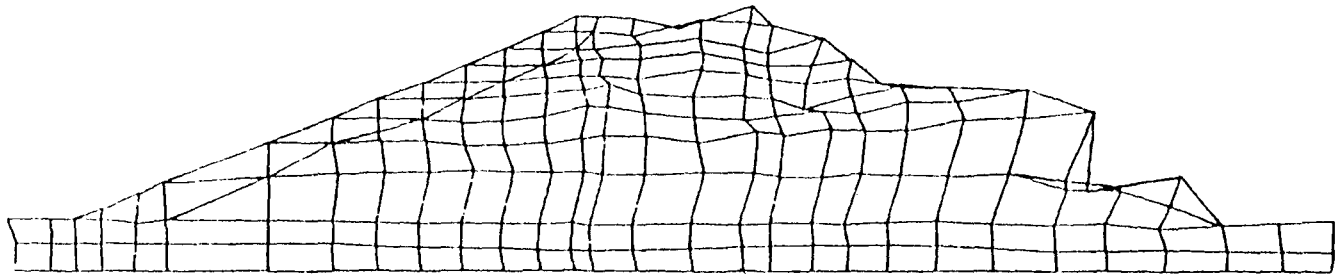


Figure 22. – Hyperbolic prediction for time 0.630 second – Sheffield Dam.

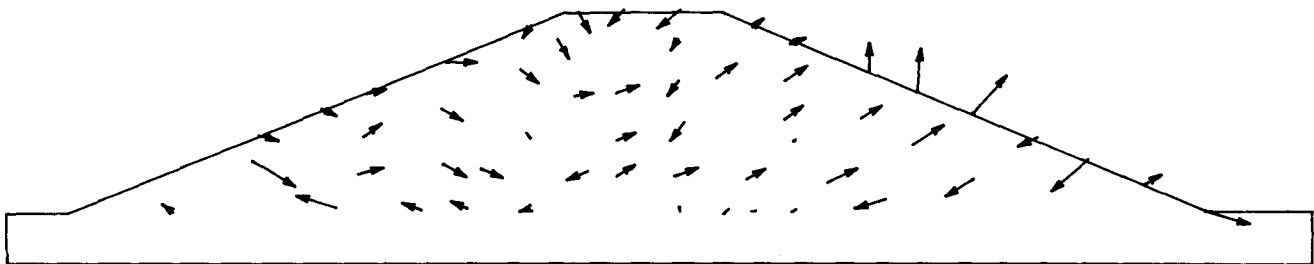


Figure 23. – Displacement vectors for hyperbolic prediction for time 0.630 second – Sheffield Dam.

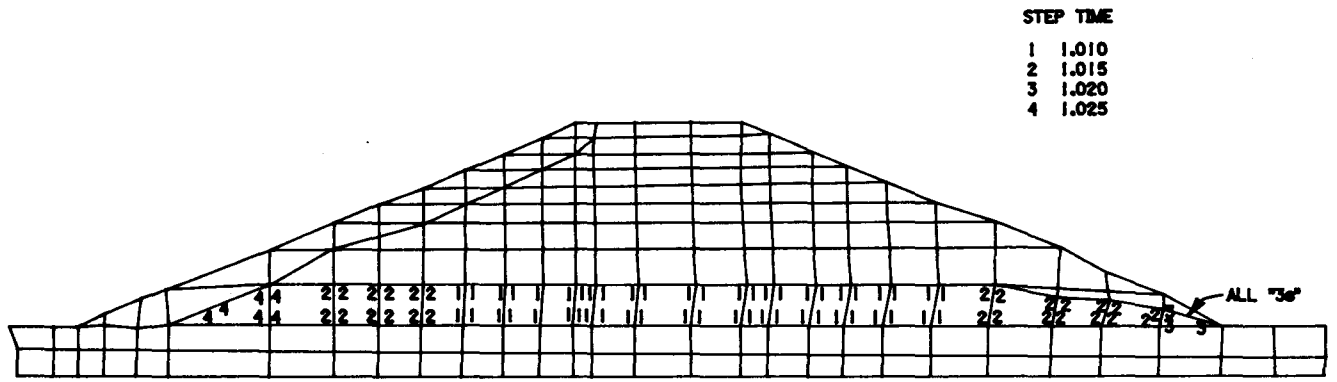


Figure 24. – Model of liquefaction progression for Sheffield Dam.

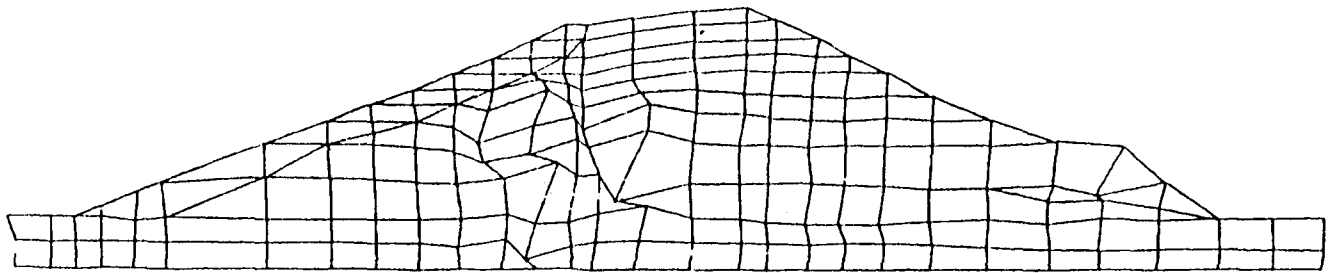


Figure 25. – Cap model prediction for time 0.405 second – Sheffield Dam.

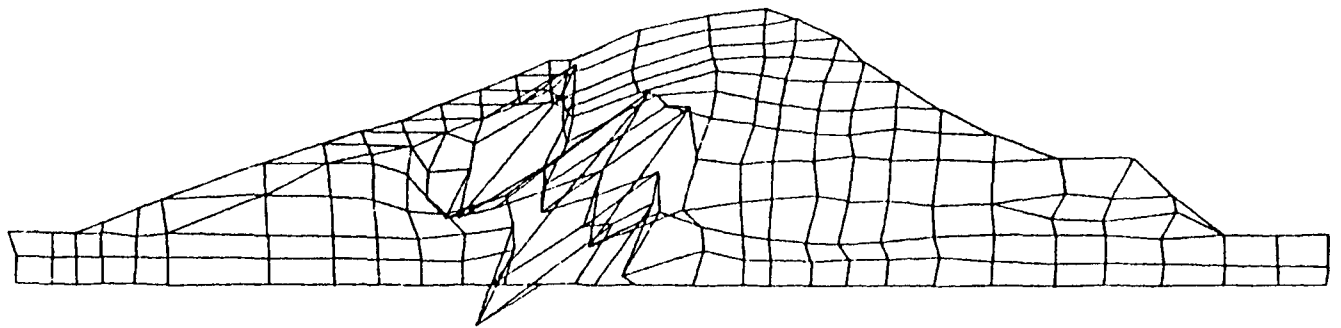


Figure 26. – Cap model prediction for time 0.430 second – Sheffield Dam.

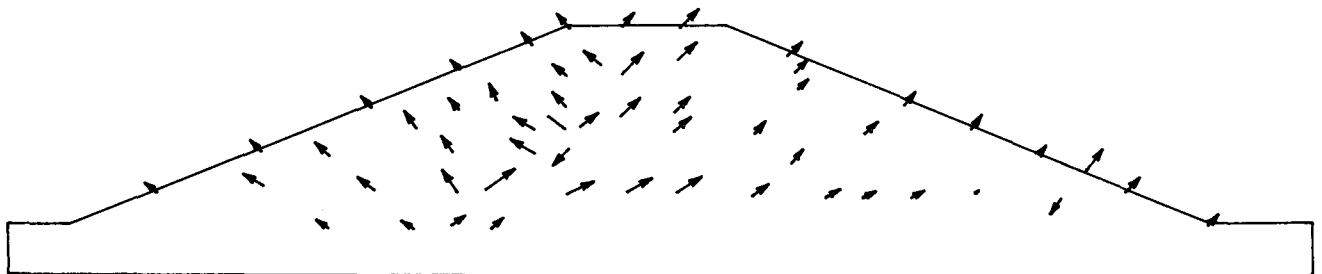


Figure 27. – Displacement vectors for cap model prediction for time 0.430 second – Sheffield Dam.

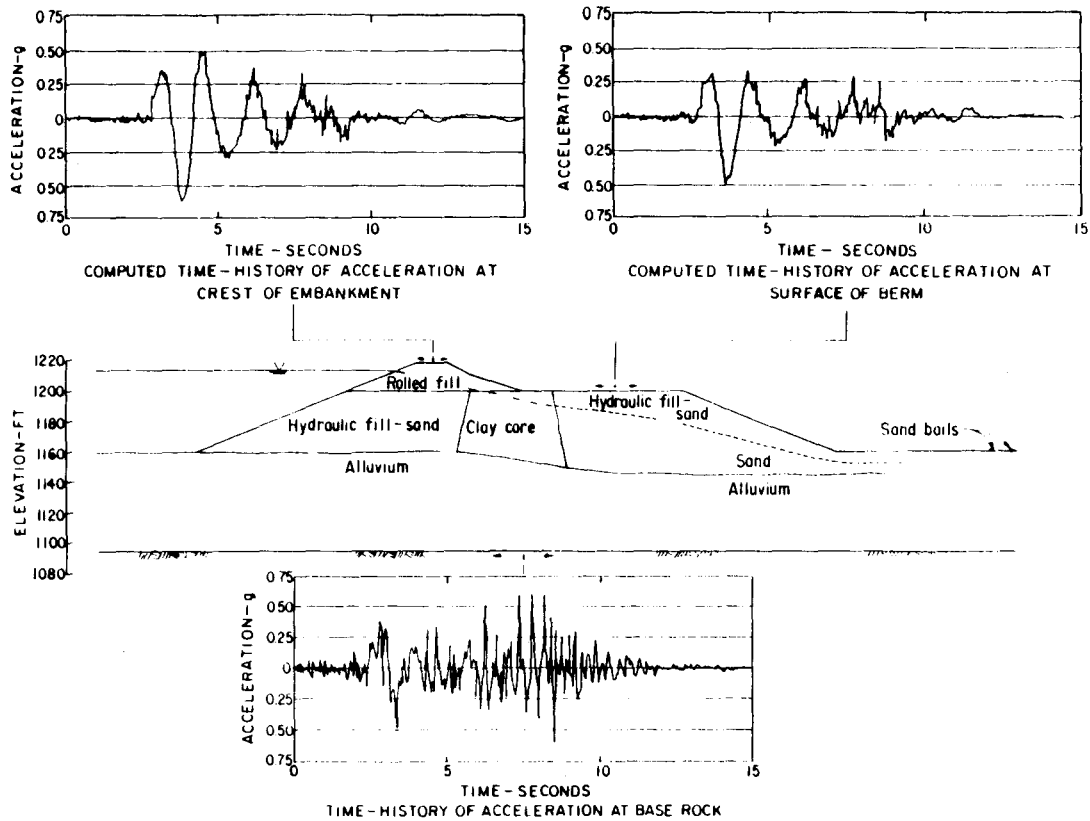


Figure 28. — Maximum cross section and earthquake record of Lower San Fernando Dam. From [22].

earthquake was 8½ miles from the dam and about 8 miles deep. A thrust faulting that occurred during the earthquake had features resembling a fault break traced to the eastern edge of Lower Van Norman Reservoir. The strong-motion shaking was recorded during the earthquake. An accelerogram for the dam is shown on figure 28.

After the earthquake, the upstream portion of the dam was below water and below the scarp that remained only a few feet above the water. Numerous longitudinal cracks were observed downstream of the scarp and at lower elevations. Seepage through the embankment was turbid after the earthquake, but cleared within 36 hours. Piezometric pressures rose but returned to normal or lower as the reservoir elevation dropped. It was surmised from observations that a major zone of material within the dam liquefied. This zone was contained within a zone of the dam that was not liquefied. As movement began, the outer zone broke into blocks and was transported downstream. An interpretation of the failure is shown on figure 29 [22].

Recent centrifugal model tests by Scott [20] show failures on dry embankments that are similar to the Lower San Fernando Dam failure. Conclusions based on this work are that shear distortions occur during earthquake loading with subsequent volume

changes. It is these volume changes that result in pore pressure increases. This pore pressure generation method is completely consistent with the calculation procedures used in the finite element method presented in this report.

Material strengths used in the analysis are shown in table 8. Figure 30 shows the results using the hyperbolic model superimposed on the Seed et al. [22] interpretation of the failure of the dam (fig. 29). On figure 30, it can be seen that the crest of the dam moves significantly upstream and the head of the displacement is on the downstream slope. A steep backrest angle and discontinuity at the head of the slide are not modeled exactly because of continuity within the element connectivities. However, the location of the head of the slide and the loss of the crest are approximated well by this model. Downstream, a bulging of the slope that simulates the actual field phenomena is modeled. The flow of material at the toe, forming a mound, is not predicted with the model because of the continuity of elements and small deformation theory. Within the dam, shears and vertical distortions closely model the field case. Overall, the simulation using the hyperbolic model is quite good.

Results shown on figure 30 are for the time 2.5 seconds after the beginning of the earthquake. After this

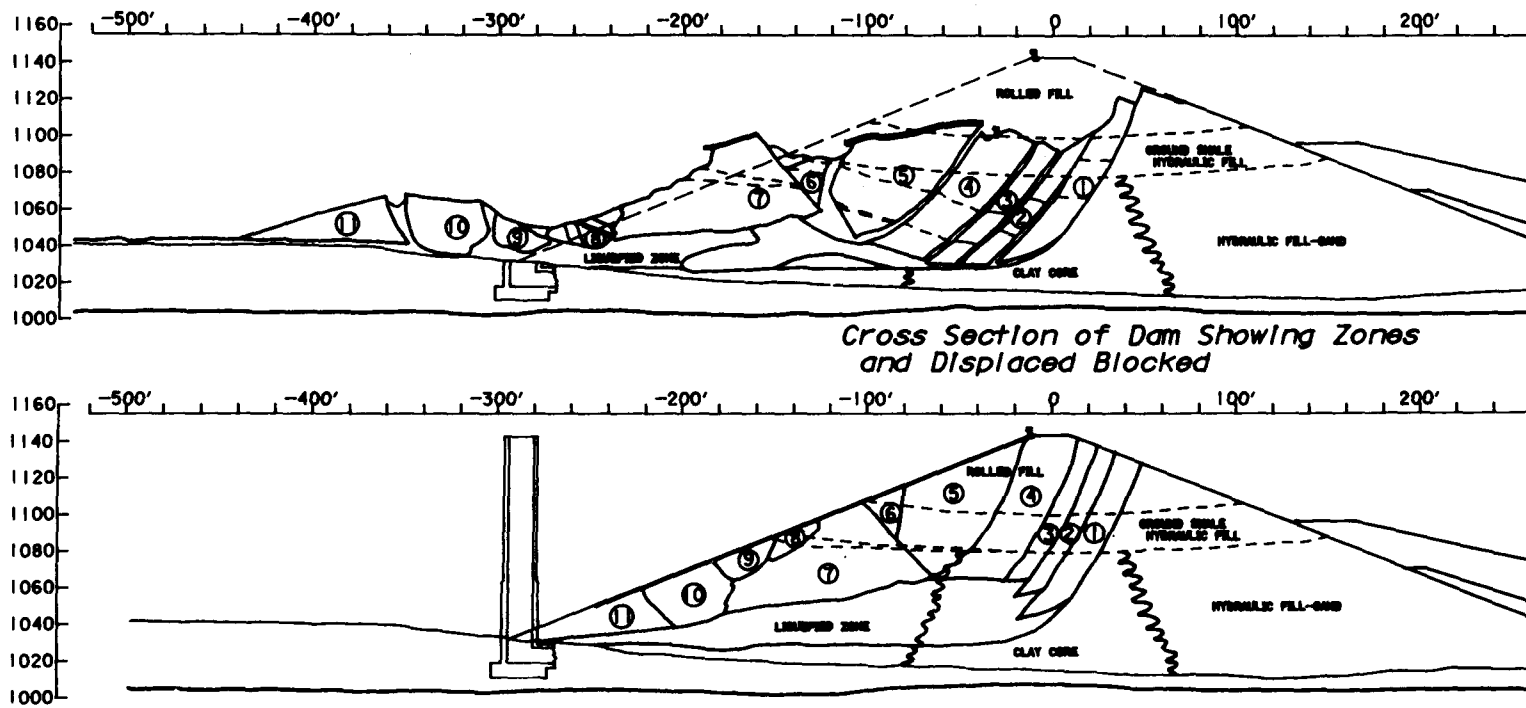


Figure 29. - Interpretation of the Lower San Fernando Dam failure. From [22].

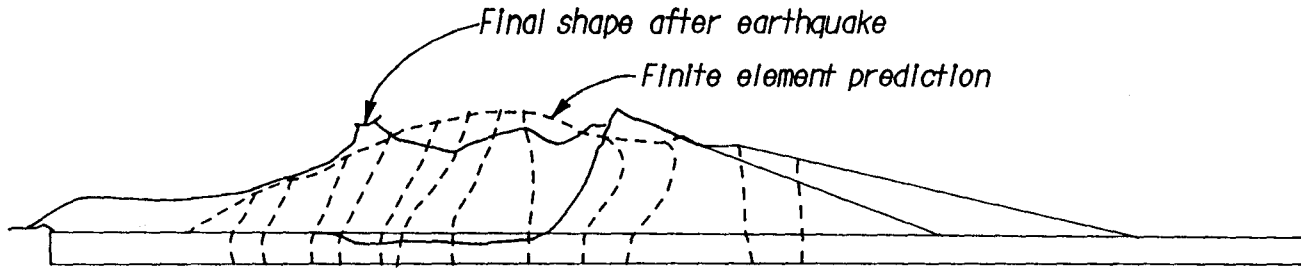


Figure 30. – Hyperbolic prediction with interpreted failure – Lower San Fernando Dam.

time the model continues to deflect and becomes numerically unstable. Therefore, the deflection at 2.5 seconds is the greatest the model can predict. The small deflection theory within this model and the use of a continuum approximation cannot be expected to model ground flow. It is not known at exactly which point in the earthquake the major failure occurred. This time (2.5 seconds) represents the first peak in the acceleration, but this is not the maximum acceleration of the record. If the blocks within the dam did indeed move at this time, then further movement was prohibited by failure to transmit load and shear distortion through a layer of liquefied material at the base of the dam. Seed et al. [22] theorize that such a layer did exist below the displaced material.

Displacement vectors for the hyperbolic model are shown on figure 31. Vectors of larger magnitude are shown at the crest, on the downstream slope, and at the toe of the movement on the upstream slope. These regions of movement are consistent with the idea of blocks being formed as shown on figure 29. Only the final cross section, discussed previously, can be used in a quantitative comparison with measured results.

The cap model predicts a similar phenomenon for the failure, as can be seen on figure 32. A downstream area is also predicted as failing (fig. 32). Such a failure was not noted during the actual field case, but is generated in this model by the crudely estimated material properties. Again, in this case later times produce very large deformations. However, a reasonable prediction can be seen before the numerical instability.

Figure 33 shows displacement vectors computed using the cap model. These vectors indicate that different blocks of material are moving in the mass. As before, this is consistent with figure 29, but cannot be verified quantitatively.

### Upper San Fernando Dam

Upper San Fernando Dam was constructed in the same region and time span as Lower San Fernando Dam, and it was constructed in approximately the same way. The embankment was placed directly on

alluvial soil. Recent deposits of alluvium in the foundation of the dam consist of a 50- to 60-foot layer of stiff clays and clayey gravels. Below the alluvium and in the abutments are poorly cemented conglomeritic sandstones and coarse-grained sandstones. The main body of the dam was placed using ponding techniques to elevation 1200.0 in 1921. An elevation of 1218.0 feet was reached by placing compacted dry fill on the upstream side. A cross section of the embankment maximum cross section is shown on figure 34.

At the time of the earthquake, the elevation of the reservoir was approximately 1213 feet. This represents a head of approximately 70 feet.

Damage in the dam resulted in a movement at the crest of 5 feet downstream with a 3-foot drop. In addition, longitudinal cracks were observed running the entire length of the dam. At the downstream toe of the dam, a 2-foot-high pressure ridge developed. Noticeable downstream movements occurred on structures in the dam. Water levels in piezometers observed during and immediately after the earthquake are of particular interest. The effect of the shaking was an immediate rise in water levels. The rises recorded were measured after the earthquake and ranged from 8.5 to 17.0 feet of water. In the center of the dam, water levels exceeded the top elevation of the piezometers and could not be recorded. Observations suggest that high pore pressures and lowered strengths were the reason for the movements in the dam.

Hyperbolic material properties used for the Upper San Fernando Dam analysis were taken from parameters used by Seed, et al. [22]. Cap parameters were calculated or chosen as discussed for Oroville Dam. Values used are shown in table 9. Pore pressure parameters were the same as for Lower San Fernando Dam. The hydraulic fill was considered as a liquefiable zone.

A downstream slide displacing the crest approximately 6 feet will provide a correct prediction. Thus, this case history tests the ability to apply both the nonlinear models and the pore pressure model and not induce a complete failure of the mesh. This tests

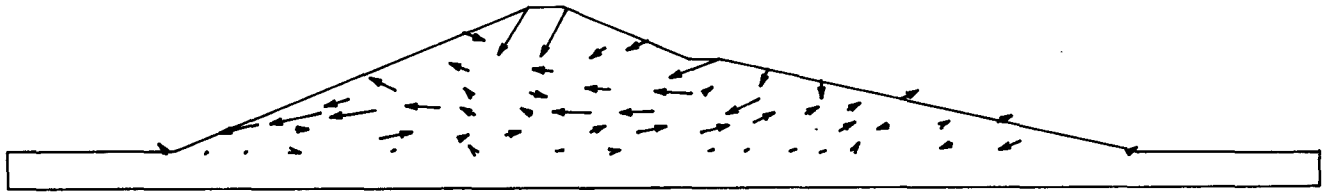


Figure 31. – Displacement vectors for hyperbolic prediction – Lower San Fernando Dam.

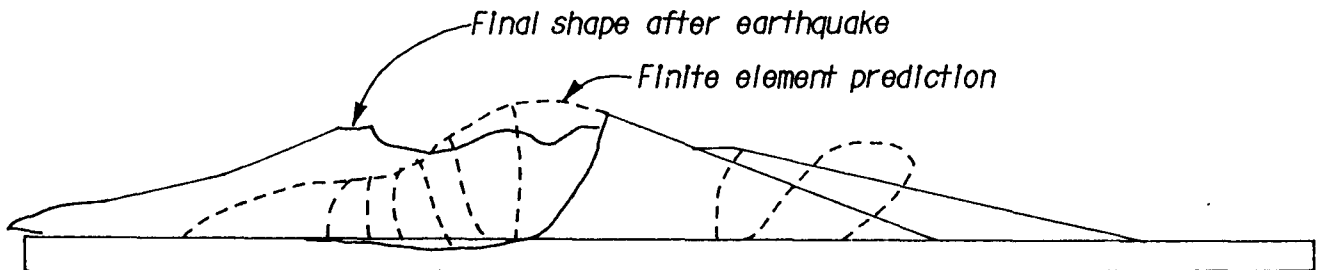


Figure 32. – Cap prediction with interpreted failure.

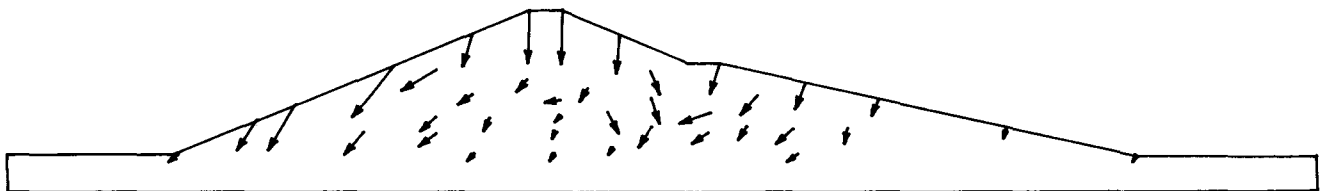


Figure 33. – Displacement vectors for cap model – Lower San Fernando Dam.

the final predictive capability necessary for the models.

The hyperbolic model displacement prediction is shown on figures 35 and 36 for times 0.13 and 0.18 second, respectively. From these figures it can be seen that the outset of failure is clearly in the downstream direction. On figure 36, note the development of a zone of disruption in the downstream toe and foundation contact. However, the distortion of the mesh incorrectly shows a complete failure.

Results for the cap model at time 0.705 second are shown on figure 37. The strain-hardening capability of the model allows displacement, as noted by the downstream bulge, without becoming rigid plastic and numerically unstable. In addition, when the plastic volumetric strains become large the elastic Young's modulus is used to avoid numerical instability. This allows approximations for conditions after shear collapse with high tensile loadings. Typical displacements using this technique are shown on figure 38 for time 2.955 seconds. The first major acceleration peak of the earthquake has passed by this time. As can be seen on figure 31, displacements can be large with large loads using this technique,

and a stiffer modulus may be appropriate. The use of small deflection theory can be inappropriate in these cases. A special condition flag is printed with the output to allow users to interpret results. Figure 39 portrays displacement vectors using the cap model. For this case, a clear rotational type mass moving downstream is evident. From the cross section that existed after the failure, this is the probable mode of movement.

## CONCLUSIONS

The finite element analysis method presented can be used to model effective stress phenomena during static and dynamic loading. Both laboratory tests and actual dams subjected to earthquakes were analyzed and reasonable predictions were found for displacements and liquefactions. The method uses a single program, eliminating the need (and assumptions involved) for several independent computer codes.

The finite element method produces failure and non-failure predictions and a wealth of stress, pore pressure, and displacement information. The use of small deformation theory is a limitation, but reasonable

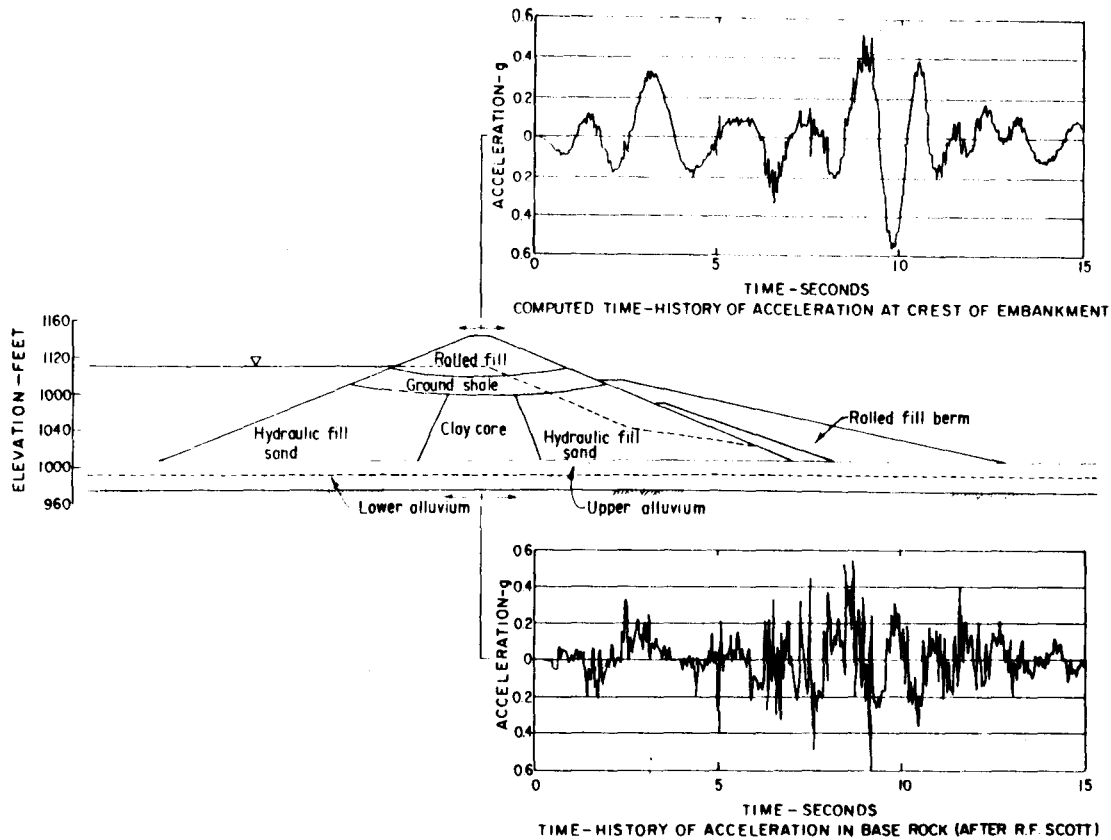


Figure 34. – Maximum cross section and earthquake record of Upper San Fernando Dam. From [22].

predictions were made for all cases in this report in spite of this limitation. Thus, a complete solution of all parameters is found within a single analysis. Another advantage of the finite element method is that it predicts displacements, stresses, and pore pressures, all of which are measurable in the field. Thus, it is possible throughout the life of the structure to study observed phenomena with finite element procedures. Furthermore, failure is not necessary to check predictions with actual field cases.

The disadvantages to the finite element method are the amount of work required to prepare the input, the volume of output that can be produced, and the computer time required to perform the analysis. However, for major structures, these investments are clearly small compared with the cost of the project.

The benefit gained in understanding the behavior of the structure definitely warrants the use of the finite element analysis method.

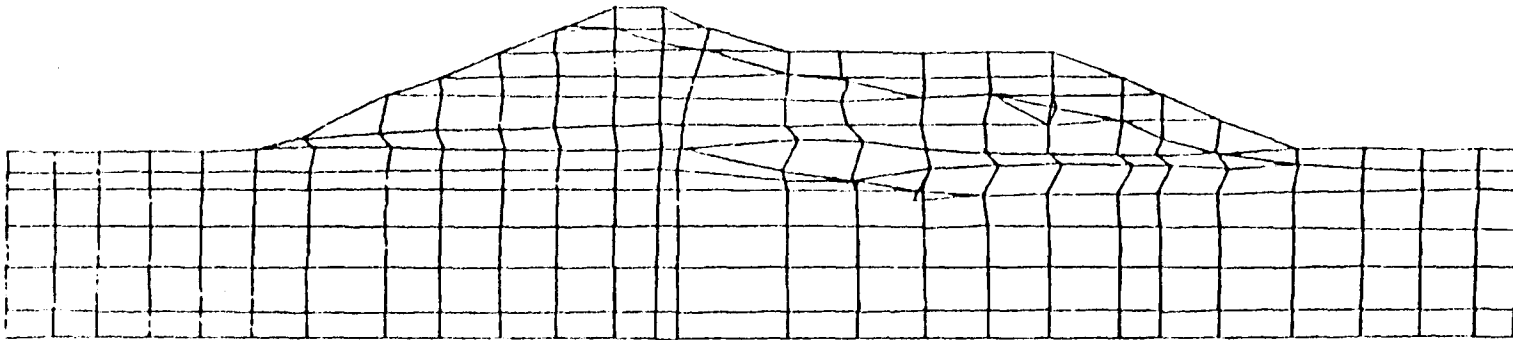


Figure 35. – Hyperbolic prediction for time 0.13 second – Upper San Fernando Dam.

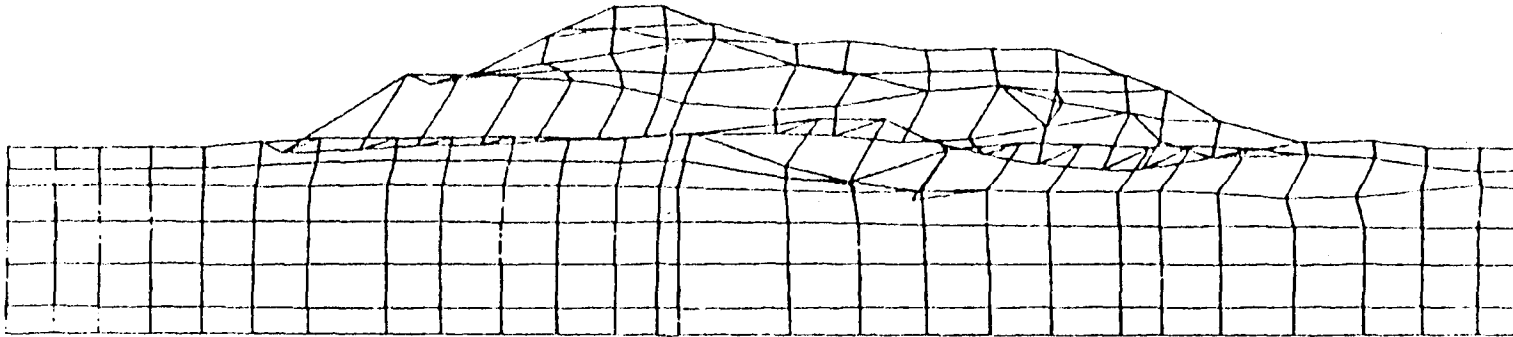


Figure 36. – Hyperbolic prediction for time 0.18 second – Upper San Fernando Dam.

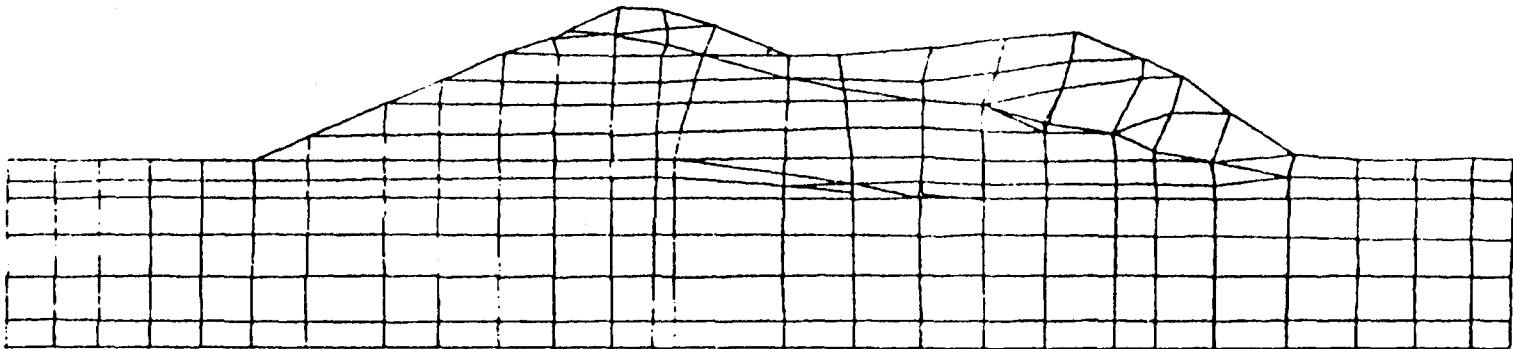


Figure 37. – Cap prediction for time 0.705 second – Upper San Fernando Dam.

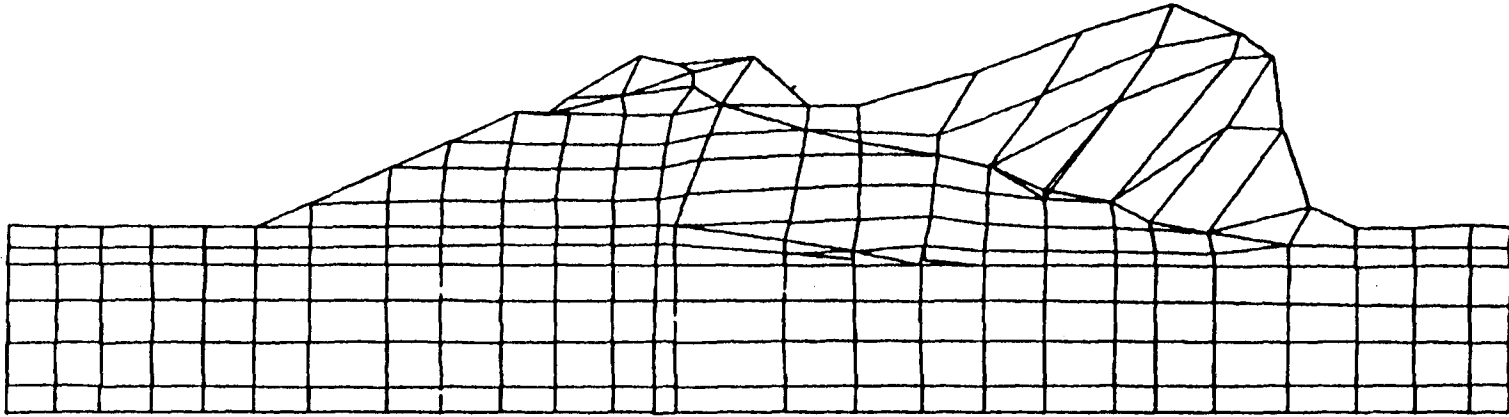


Figure 38. – Cap prediction for time 2.955 seconds – Upper San Fernando Dam.

28

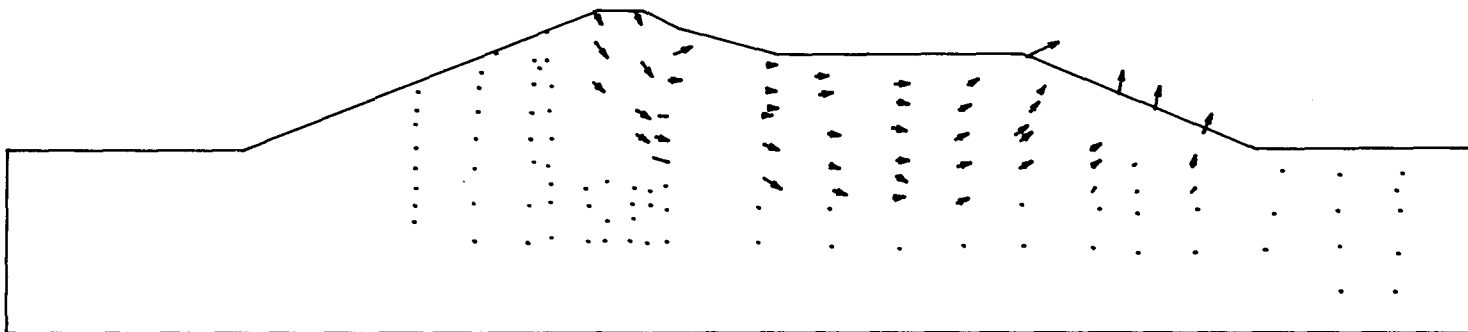


Figure 39. – Displacement vectors for cap model – Upper San Fernando Dam.

Table 1. – Cyclic triaxial test results – Sample B2-100-2. From [3].

No. of cycles	$\frac{\Delta u^*}{\sigma'_{vo}}$	$\frac{\sigma_d}{2}$	Double amp. shear strain		$\zeta, \%$	$\Sigma \zeta$	$\kappa$
			Strain, %	$\gamma_{max} = 1.5 \varepsilon_{ar}, \%$			
1	0.20	0.20	0.00	0.00	0.00	0.000	0.00
2	.27	.20	.20	.30	.60	.006	.87
3	.31	.20	.40	.60	1.20	.018	2.60
4	.36	.20	.60	.90	1.80	.036	5.20
5	.40	.20	.60	.90	1.80	.054	7.79
6	.44	.20	.60	.90	1.80	.072	10.39
7	.49	.20	.80	1.20	2.40	.096	13.85
8	.53	.20	.80	1.20	2.40	.12	17.32
9	.58	.20	1.40	2.10	4.20	.162	23.38
10	.64	.20	2.40	3.60	7.20	.234	33.77
11	.72	.20	6.40	9.60	19.20	.426	61.48
12	.79	.20	15.70	23.55	47.10	.897	129.46
13	.83	.20	–	–	–	–	–

\*  $\sigma'_{vo} = 30 \text{ lb/in}^2$ .

Table 2. – Cyclic triaxial test results – Sample B2-100-3. From [3].

No. of cycles	$\frac{\Delta u^*}{\sigma'_{vo}}$	$\frac{\sigma_d}{2}$	Double amp. shear strain		$\zeta, \%$	$\Sigma \zeta$	$\kappa$
			Strain, %	$\gamma_{max} = 1.5 \varepsilon_{ar}, \%$			
1	0.13	0.19	0.40	0.60	1.20	0.012	1.35
2	.20	.19	.40	.60	1.20	.024	2.70
3	.24	.19	.40	.60	1.20	.036	4.05
4	.29	.19	.40	.60	1.20	.048	5.40
5	.33	.19	.60	.90	1.80	.066	7.43
6	.37	.19	.60	.90	1.80	.084	9.45
7	.40	.19	.60	.90	1.80	.102	11.48
8	.44	.19	.80	1.20	2.40	.126	14.18
9	.48	.19	.80	1.20	2.40	.150	16.88
10	.52	.19	1.00	1.50	3.00	.180	20.26
11	.57	.19	1.00	1.50	3.00	.21	23.64
12	.61	.19	1.20	1.80	3.60	.246	27.69
13	.67	.19	1.80	2.70	5.40	.30	33.77
14	.73	.19	2.79	4.19	8.38	.3838	43.20
15	.81	.19	6.58	9.87	19.74	.5812	65.41
16	.87	.19	13.97	20.96	41.92	1.0004	1126.0
17	.89	.19	23.54	35.31	70.62	1.7066	192.08

\*  $\sigma'_{vo} = 30 \text{ lb/in}^2$ .

Table 3. – Cyclic triaxial test results – Sample B2-100-4. From [3].

No. of cycles	$\frac{\Delta u^*}{\sigma'_{vo}}$	$\frac{\sigma_d}{2}$	Double amp. shear strain		$\zeta, \%$	$\Sigma \zeta$	$\kappa$
			Strain, %	$\gamma_{max} = 1.5 \varepsilon_{ar}, \%$			
1	0.23	0.23	1.00	1.50	3.00	0.030	9.13
2	.57	.23	5.60	8.40	16.80	.198	60.29
3	.90	.23	24.00	36.0	72.00	.918	279.28

\*  $\sigma'_{vo} = 30 \text{ lb/in}^2$ .

Table 4. – Cyclic triaxial test results – Sample B2-100-5. From [3].

No. of cycles	$\frac{\Delta u^*}{\sigma_{vo}'}$	$\frac{\sigma_d}{2}$	Double amp. shear strain		$\zeta_r$ %	$\Sigma \zeta$	$\kappa$
			Strain, %	$\gamma_{max} = 1.5 \varepsilon_{ar}$ %			
1	0.13	0.16	0.20	0.30	0.60	0.006	0.32
2	.17	.16	.30	.45	.90	.015	.80
3	.20	.16	.40	.60	1.20	.027	1.44
4	.22	.16	.50	.75	1.50	.042	2.24
5	.24	.16	.60	.90	1.80	.06	3.20
6	.27	.16	.62	.93	1.86	.0786	4.20
7	.29	.16	.63	.95	1.90	.0976	5.21
8	.31	.16	.64	.96	1.92	.1168	6.24
9	.33	.16	.66	.99	1.98	.1366	7.29
10	.34	.16	.67	1.01	2.02	.1568	8.37
11	.35	.16	.68	1.02	2.04	.1772	9.46
12	.37	.16	.70	1.05	2.10	.1982	10.58
13	.38	.16	.71	1.07	2.14	.2196	11.72
14	.40	.16	.73	1.10	2.20	.2416	12.90
15	.41	.16	.74	1.11	2.22	.2638	14.08
16	.43	.16	.75	1.13	2.26	.2864	15.29
17	.44	.16	.76	1.14	2.28	.3092	16.51
18	.46	.16	.77	1.16	2.32	.3324	17.75
19	.47	.16	.78	1.17	2.34	.3558	19.00
20	.49	.16	.79	1.19	2.38	.3796	20.29
21	.50	.16	.80	1.20	2.40	.4036	21.55
22	.52	.16	.83	1.25	2.50	.4286	22.88
23	.53	.16	.86	1.29	2.58	.4544	24.26
24	.55	.16	.89	1.34	2.68	.4812	25.69
25	.57	.16	.92	1.38	2.76	.5088	27.16
26	.59	.16	.95	1.42	2.84	.5372	28.68
27	.60	.16	.99	1.48	2.96	.5668	30.26
28	.62	.16	.99	1.48	2.96	.5964	31.84
29	.64	.16	.99	1.48	2.96	.626	33.42
30	.66	.16	1.10	1.65	3.30	.659	35.18
31	.69	.16	1.2	1.80	3.60	.695	37.11
32	.72	.16	1.5	2.25	4.50	.74	39.51
33	.75	.16	1.80	2.70	5.40	.794	42.39
34	.79	.16	3.1	4.65	9.30	.887	47.36
35	.82	.16	4.4	6.60	13.20	1.019	54.40
36	.85	.16	8.15	12.23	24.46	1.2636	67.46
37	.87	.16	11.9	17.85	35.70	1.6206	86.52
38	.89	.16	18.5	27.75	55.50	2.1756	116.16
39	.90	.16	22.0	33.00	66.00	2.8356	151.39

\*  $\sigma_{vo}' = 30 \text{ lb/in}^2$ .

Table 5. – Cyclic triaxial test results – Sample B2-100-6. From [3].

No. of cycles	$\frac{\Delta u^*}{\sigma_{vo}'}$	$\frac{\sigma_d}{2}$	Double amp. shear strain			$\Sigma \zeta$	$\kappa$
			Strain, %	$\gamma_{max} = 1.5 \varepsilon_a$ , %	$\zeta$ , %		
1	0.17	0.23	0.20	0.30	0.60	0.006	1.83
2	.26	.23	.40	.60	1.20	.018	5.48
3	.33	.23	.60	.90	1.80	.036	10.95
4	.38	.23	.80	1.20	2.40	.06	18.25
5	.43	.23	1.00	1.50	3.00	.09	27.38
6	.50	.23	1.20	1.80	3.60	.126	38.33
7	.57	.23	1.40	2.10	4.20	.168	51.11
8	.65	.23	2.00	3.00	6.00	.228	69.36
9	.77	.23	4.44	6.60	13.20	.360	109.52
10	.87	.23	12.00	18.00	36.00	.72	219.05
11	.89	.23	22.00	33.00	66.00	1.38	419.84

\*  $\sigma_{vo}' = 30 \text{ lb/in}^2$ .

Table 6. – Oroville Dam strength parameters.

Parameter	Zone				
	Shell	Transition	Core	Concrete	Foundation
Unit weight, lb/ft <sup>3</sup>	150	150	150	162	
Strength parameters,					
<i>c</i> , lb/ft <sup>2</sup>	0	0	2,640	4,320	
$\phi^\circ$	43.5	43.5	25.1	0	
Linear parameters					
<i>E<sub>i</sub></i> , lb/ft <sup>2</sup>					360,000,000
<i>v</i>					0.27
Hyperbolic parameters					
<i>K</i>	3,780	3,350	345	137,500	
<i>n</i>	0.19	0.19	0.76	0	
<i>R<sub>f</sub></i>	.76	.76	.88	1.0	
<i>K<sub>b</sub></i>	175	100	145	40,000	
<i>m</i>	0.2	0.2	0.2	0.0	
<i>K<sub>ur</sub></i>	9,000	3,000	1,000	30,000	
<i>E<sub>i</sub></i> , lb/ft <sup>2</sup>	30,711,460	30,711,460	30,711,460	1,000,000,000	
<i>B<sub>i</sub></i> , lb/ft <sup>2</sup>	10,000,000	10,000,000	10,000,000	300,000,000	
Cap model					
Type (1=soil)	1	1	1		
Tension cutoff, lb/ft <sup>2</sup>	0	0	0		
<i>E<sub>i</sub></i> , lb/ft <sup>2</sup>	12,789,411	11,334,531	4,772,073		
<i>v<sub>i</sub></i>	0.25	0.25	0.25		
<i>CA</i>	28,896	28,896	28,896		
<i>CB</i>	0.8	0.8	0.8		
<i>CC</i>	28,896	28,896	30,940		
<i>CR</i>	4.76	4.76	8.13		
<i>CD</i>	0.001	0.001	0.001		
<i>CW</i>	.001	.001	.001		
<i>X<sub>int</sub></i>	-50,050	-50,050	-50,050		

Table 7. – Sheffield Dam strength parameters.

Parameter	Zone		
	All soil above	All soil below	Foundation
Unit weight, lb/ft <sup>3</sup>	107	120	120
Strength parameters,			
<i>c</i> , lb/ft <sup>2</sup>	512	205	--
$\phi^\circ$	26	13	--
Linear parameters			
<i>E<sub>v</sub></i> , lb/ft <sup>2</sup>			3,279,741
<i>v</i>			0.25
Hyperbolic parameters			
<i>K</i>	800	800	
<i>n</i>	0.33	0.33	
<i>R<sub>r</sub></i>	0.62	0.62	
<i>K<sub>b</sub></i>	650	650	
<i>m</i>	0	0	
<i>K<sub>ur</sub></i>	1,600	1,600	
<i>E<sub>v</sub></i> , lb/ft <sup>2</sup>	3,250,000	3,250,000	
<i>B<sub>v</sub></i> , lb/ft <sup>2</sup>	1,000,000	1,000,000	
Cap model			
Type (1=soil)	1	1	
Tension cutoff, lb/ft <sup>2</sup>	0	0	
<i>E<sub>v</sub></i> , lb/ft <sup>2</sup>	3,279,740	3,279,740	
<i>v<sub>i</sub></i>	0.25	0.25	
<i>CA</i>	938	938	
<i>CB</i>	0.8	0.8	
<i>CC</i>	1,117	1,336	
<i>CR</i>	7.902	1,486	
<i>CD</i>	0.001	0.001	
<i>CW</i>	0.001	0.001	
<i>X<sub>int</sub></i>	-1,625	-1,625	
Endochronic pore pressure constants			
<i>A</i>		2,914	
<i>B</i>		1,904	
<i>κ</i>		0.046	

Table 8. - Lower San Fernando Dam strength parameters.

Parameter	Zone					
	Rolled fill	Ground shale	Rolled berm	Hydraulic fill	Clay core	Foundation
Dry unit weight, $\gamma_d$	125	106	125	106	106	110
Buoyant unit weight, $\gamma_b$	78	64	78	64	64	68
Strength parameters,						
$c$ , lb/ft <sup>2</sup>	2,600	0	2,600	0	0	0
$\phi^\circ$	25	37	25	37	37	38
Linear parameters, lb/ft <sup>2</sup>						
$E_p$ , lb/ft <sup>2</sup>						30,711,500
$\nu$						0.41
Hyperbolic parameters						
$K$	300	510	300	510	510	
$n$	0.76	0.54	0.76	0.54	0.54	
$R_f$	.90	.72	.90	.72	.71	
$K_b$	750	1,900	740	1,900	1,900	
$m$	-0.96	-1.1	-0.76	-1.1	-1.1	
$K_{ur}$	900	1,260	900	1,260	1,260	
$E_i$ , lb/ft <sup>2</sup>	100,000	32,433	100,000	32,433	32,433	
$B_i$ , lb/ft <sup>2</sup>	33,333	10,811	33,333	10,811	10,811	
Cap model						
Type (1=soil)	1	1	1	1	1	
Tension cutoff, lb/ft <sup>2</sup>	0	0	0	0	0	
$E_i$ , lb/ft <sup>2</sup>	100,000.	973,000.	100,000.	973,000.	973,000.	
$\nu_i$	0.30	0.33	0.30	0.33	0.33	
CA	600.0	6,000.0	600.0	6,000.0	6,000.0	
CB	0.8	0.8	0.8	0.8	0.8	
CC	3,200.0	6,000.0	3,200.0	6,000.0	6,000.0	
CR	5.32	5.32	5.32	5.32	5.32	
CD	0.001	0.001	0.001	0.001	0.001	
CW	.001	.001	.001	.001	.001	
$X_{int}$	-7,200.0	-7,200.0	-7,200.0	-7,200.0	-7,200.0	
Endochronic pore pressure constants						
A				2,914		
B				1,904		
$\kappa$				0.046		

Report No. EERC 73-2, College of Engineering,  
University of California, Berkeley, CA, 1973.

[23] Vrymoed, J., "Dynamic FEM Model of Oroville Dam," *Journal of the Geotechnical Division, Proceedings of the ASCE*, No. GT8, pp. 1057-1077, 1981.

[24] Wong, K. S., and J. M. Duncan, *Hyperbolic Stress-Strain Parameters for Nonlinear Finite Element Analyses of Stresses and Movements in Soil Masses*, Institute of Transportation and Traffic Engineering, University of California, Berkeley, CA, 1974.

**APPENDIX A**  
**TYPICAL HYPERBOLIC MODEL CONSTANTS FOR DAMS**



Table A.1. – Hyperbolic parameters for drained conditions. From [24].

Soil	Soil description	Init. void ratio	Relative density	Stress range (TSF)	C (TSF)	Friction angle	K	n	R <sub>f</sub>	K <sub>b</sub>	m
GW	Conglomerate Rockfill (Netzahu. Dam)	0.39	70	1.9 - 25.5	0.	50 (10)	540	0.43	0.64	135	0.34
GW	Granitic Gneiss Rockfill (Mica Dam)	0.32	95	5.1 - 25.6	0.	44 (9)	210	0.51	0.64	100	0.34
GW	Quartzite Rockfill (Furnas Dam Shell)			4.1 - 36.9	0.	49 (6)	560	0.48	0.65	330	0.33
GW	Quartzite Rockfill (Furnas Dam Transit)			4.1 - 36.9	0.	53 (7)	950	0.52	0.59	470	0.52
GW	Furnas Dam Transition			4.1 - 36.9	0.	50 (7)	690	0.57	0.51	360	0.57
GW	Pinzandapan Gravel	0.34	65	0.4 - 26.5	0.	51 (9)	690	0.45	0.59	170	0.22
GW	Diorite Rockfill (El Infiernillo Dam)	0.56	50	0.4 - 17.0	0.	46 (9)	340	0.28	0.71	52	0.18
GP	Sandy Gravel (Mica Dam Shell)		50	7.2 - 32.5	0.	41 (3)	420	0.50	0.78	125	0.46
GP	Basalt Rockfill	0.3	95	5.1 - 25.6	0.	52 (10)	450	0.37	0.61	255	0.18
GP	Silty Sandy Gravel (Oroville Dam)	0.21	100	9.0 - 46.8	0.	53 (8)	1300	0.40	0.72	900	0.22
GP	Amphibolite Gravel (Oroville Dam Shell)	0.2	100	2.2 - 28.6	0.	51 (6)	1780	0.39	0.67	1500	0.16
GP	Crushed Basaltic Rock (Round Butte Dam)		99	2.0 - 14.1	0.	51 (14)	410	0.21	0.71	195	0
GP	Sandy Gravel (Rowan Dam)	0.233	100	1.8 - 10.8	0.	58 (10)	2500	0.21	0.75	1400	0
GC	Clayey Gravel (New Hogan Dam Core)			1.1 - 4.3	0.28	19	99	0.70	0.86	45	0
SW	Argillite Rockfill (Pyramid Dam Shell)	0.46	100	2.2 - 46.8	0.	53 (9)	1600	0.08	0.72	600	0
SW	Crushed Olivine Basalt	0.43	100	2.2 - 46.8	0.	55 (10)	1000	0.22	0.70	390	0.14
SW	Silty Sand, Some Gravel (Round Butte Dam)			2.0 - 14.0	0.	38 (3)	260	0.50	0.76	100	0.5
SW	Venato Sandstone (0.5 in. max. size)	0.47	93	2.2 - 28.6	0.	43 (4)	330	0.46	0.51	110	0.46
SP	Glacial Cutwash Sand	0.5	80	1.0 - 41.1	0.	44 (4)	190	0.70	0.57	190	0.35
SP	Sacramento River Sand	0.87	38	1.0 - 41.1	0.	35 (2)	430	0.27	0.84	230	0.02
SP	Sacramento River Sand	0.78	60	1.0 - 13.0	0.	37 (2)	410	0.69	0.90	260	0.15
SP	Sacramento River Sand	0.71	78	1.0 - 41.1	0.	41 (5)	1100	0.36	0.85	900	0
SP	Sacramento River Sand	0.61	100	3.0 - 41.1	0.	45 (7)	1200	0.48	0.85	1500	0
SP	Ham River Sand	0.82	loose	7.2 - 287.9	0.	31 (2)	890	0.26	0.78	360	0.11
SP	Ham River Sand	0.64	dense	7.2 - 71.3	0.	47 (9)	1100	0.57	0.86	2250	0
SP	Poorly Graded Sand (Port Allen Lock)	0.73	49	0.9 - 3.9	0.	39 (0)	410	0.65	0.84		
SP	Poorly Graded Sand (Port Allen Lock)	0.65	73	0.9 - 3.9	0.	40 (1)	400	0.49	0.77		
SP	Poorly Graded Sand (Port Allen Lock)	0.57	98	0.9 - 3.9	0.	44 (4)	750	0.77	0.83		
SP	Coarse to Fine Sand (Round Butte Dam)	1.22	70	2.0 - 14.0	0.	39 (6)	280	0.37	0.71	95	0.21
SP	Fumicecus Sand (Round Butte Dam)		77	2.0 - 14.1	0.	48 (10)	340	0.45	0.70	230	0.06
SP	Fumicecus Sand (Round Butte Dam)		71	2.0 - 14.1	0.	49 (12)	650	0.38	0.77	380	0.05

Table A.1. – Hyperbolic parameters for drained conditions. From [24]. – Continued

Soil	Soil description	Init. void ratio	Relative density	Stress range (TSF)	C (TSF)	Friction angle	K	n	R <sub>f</sub>	K <sub>b</sub>	m
SP	Fine Silica Sand (Loose)	0.65	38	1.0 - 5.1	0.	30 (0)	280	0.65	0.93	110	0.65
SP	Fine Silica Sand (Dense)	0.54	100	1.0 - 5.1	0.	37 (9)	1400	0.74	0.90	1080	0.15
SP	Monterey No. 0 Sand (Cylind. specimen)	0.78	27	0.3 - 1.2	0.	35 (0)	920	0.79	0.96	465	0.32
SP	Monterey No. 0 Sand (Cubical specimen)	0.78	27	0.3 - 1.2	0.	39 (0)	510	0.51	0.97	370	0.22
SP	Monterey No. 0 Sand (Cylind. specimen)	0.57	98	0.3 - 1.2	0.	45 (3)	3200	0.78	0.92	1400	0.45
SP	Monterey No. 0 Sand (Cubical specimen)	0.57	98	0.3 - 1.2	0.	47 (5)	1500	0.76	0.91	1100	0.52
SP	Basaltic Sand (Round Butte Dam)			2.0 - 14.0	0.	39 (13)	1600	0.08	0.63	750	0
SM	Silty Sand (Chaffield Dam)			6.0 - 10.0	0.	37 (0)	100	1.07	0.62		
SM	Silty Gravelly Sand (Chaffield Dam)			6.0 - 10.0	0.	41 (0)	530	0.51	0.62	640	0
SM	Silty Sand w/Pebbles (Round Butte Dam)			2.0 - 14.0	0.	46 (8)	700	0.35	0.75		
SM	Silty Sand w/Pumice (Round Butte Dam)			2.0 - 13.7	0.	43 (8)	670	0.25	0.72	500	0
SM	Silty Sand (Round Butte Dam)			2.0 - 14.1	0.	36 (5)	530	0.28	0.74	470	0
SM	Silty Sand and Gravel (Round Butte Dam)			2.0 - 14.0	0.	36 (11)	800	0.20	0.67	600	0
SM-SC	Silty Clayey Sand (Mica Dam Core)			3.6 - 32.4	0.31	33	700	0.37	0.80	280	0.19
SM-SC	Silty Clayey Sand (Mica Dam Core)			3.6 - 18.0	0.85	34	425	0.58	0.70	205	0.44
SM-SC	Silty Clayey Sand (Mica Dam Core)			3.6 - 32.4	0.40	34	160	0.81	0.63	65	0.81
ML	Cannonsville Silt (Undisturbed)	0.57		1.5 - 7.4	0.	45 (6)	200	1.07	0.57	200	0.89
ML	Sandy Silty w/Pumice (Round Butte Dam)			2.0 - 13.9	0.	42 (7)	500	0.45	0.82	400	0
ML	Sandy Silty w/Pumice (Round Butte Dam)			2.0 - 13.9	0.	36 (1)	530	0.35	0.71	520	0.23
CL	Silty Clay (Canyon Dam)			1.0 - 8.2	0.17	30	550	-0.05	0.82		
CL	Silty Clay (Canyon Dam)			1.0 - 8.2	0.59	29	690	0.10	0.71		
CL	Silty Clay (Canyon Dam)			1.0 - 8.2	0.51	33	150	0.62	0.61	360	0
CL	Silty Clay (Canyon Dam)			1.0 - 4.0	0.39	30	160	0.50	0.63	210	0
CL	Silty Clay (Canyon Dam)			.5 - 8.0	0.26	31	130	0.59	0.72	45	0.59

Table A.2. – Hyperbolic parameters for undrained conditions. From [24].

Soil	Soil description	Compaction				Degree saturation	Stress range (TSF)	C (TSF)	Friction angle	K	n	R <sub>f</sub>	K <sub>D</sub>	m
		Max. dry unit wt. (lb/ft <sup>3</sup> )	Opt. w/c	Dry unit wt. (lb/ft <sup>3</sup> )	w/c									
GC	Sandy Gravel (Droville Dam Core)	138.6	8.1	139.0	8.1		3.6 - 10.9	1.50	24	540	0.51	0.84		
GC	Sandy Gravel (Droville Dam Core)	138.6	8.1	139.0	8.1		27.9 - 43.3	10.01	3	190	0.95	0.97		
SP	Poorly Graded Sand (Rodman Dam)	109.5	11.8	104.0	11.8	55	1.0 - 3.0	0.	37 (4)	590	1.10	0.89		
SP	Poorly Graded Sand (Rodman Dam)	109.5	11.8	98.6	11.8	47	1.0 - 3.0	0.	37 (8)	770	-0.14	0.87		
SP	Poorly Graded Sand (Rodman Dam)	109.5	11.8	110.0	11.2	61	1.0 - 3.0	0.	43 (9)	940	0.	0.82		
SP	Poorly Graded Silty Sand (Rodman Dam)	101.1	13.6	101.3	13.4	57	1.0 - 3.0	0.	44 (6)	420	0.67	0.76		
SP	Poorly Graded Silty Sand (Rodman Dam)	101.1	13.6	96.2	13.3	50	1.0 - 2.0	0.	44 (11)	850	0.79	0.92		
SP	Poorly Graded Silty Sand (Rodman Dam)	101.1	13.6	92.0	12.4	42	1.0 - 3.0	0.	40 (8)	470	0.51	0.86		
SM	Gravelly Silty Sand (Bell Mountain Dam)	122.9	10.0	124.0	9.4	71	1.1 - 4.35	0.	42 (5)	430	0.38	0.57		
SM	Silty Sand (Somerville Dam)	109.1	13.4	109.3	13.4	70	0.5 - 6.0	0.	40 (2)	350	0.91	0.69		
SM	Silty Sand (Somerville Dam)	109.1	13.4	104.1	13.2	60	0.5 - 6.0	0.	40 (6)	420	0.84	0.75		
SM	Silty Sand (Somerville Dam)	109.1	13.4	103.6	16.7	75	0.5 - 6.0	0.	39 (4)	340	0.64	0.72		
SM-SC	Silty Clayey Sand (Hopkinton Dam)	129.2	9.2	131.0	8.8	83	1.0 - 6.0	.98	31	320	0.35	0.86		
SC	Clayey Sand (Thomaston Dam)	123.3	12.0	122.0	12.0	85	1.1 - 4.3	.92	18	39	0.61	0.55		
SC	Clayey Sand (New Don Pedro Dam Core)	125.8	9.8	123.2	9.6	73	5.4 - 21.6	2.60	26	3900	-0.08	0.93	12000	-0.99
SC	Clayey Gravelly Sand (Proctor Dam)	120.1	11.2	126.0	8.3	70	0.5 - 1.5	1.80	4	510	0.37	0.64	250	0
SC	Clayey Sand (Chatfield Dam)	122.0	11.7	116.2	14.7	90	6.0 - 10.0	1.30	0	52	0.	0.76		
SC	Clayey Sand (Chatfield Dam)	115.0	15.0	110.0	17.0	88	6.0 - 10.0	1.10	0	250	0.	0.97		
ML	Sandy Silt (Chatfield Dam)	115.0	12.8	108.7	15.6	77	6.0 - 10.0	1.80	19	208	0.59	0.86	250	0.
ML	Sandy Silt (Chatfield Dam)	115.0	12.8	109.3	12.7	63	6.0 - 10.0	0.39	30	27	1.43	0.72		
ML	Sandy Silt (Birch Dam Shell)	108.8	13.6	104.0	11.6	53	0.5 - 6.0	0.42	31	240	0.31	0.83		
ML	Sandy Silt (Birch Dam Shell)	108.8	13.6	104.0	13.6	62	1.5 - 6.0	0.19	31	270	0.38	0.82		
ML	Sandy Silt (Birch Dam Shell)	108.8	13.6	104.0	16.6	74	1.5 - 6.0	0.54	27	100	0.84	0.77		
CL	Silty Clay (Arkabutla Dam)	110.0	18.0	108.7	16.7	81	1.0 - 12.3	0.53	29	260	0.60	0.87		
CL	Silty Clay (Arkabutla Dam)	110.0	18.0	107.0	19.5	89	1.0 - 8.2	1.20	14	39	0.48	0.58		
CL	Lean Clay (Monroe Dam)	110.5	16.4	107.1	19.1	87	0.7 - 2.9	0.95	0	66	0.	0.75		
CL	Lean Clay (Monroe Dam)	110.5	16.4	104.0	21.2	89	0.7 - 2.9	0.42	0	10	0.03	0.52		
CL	Lean Clay (Monroe Dam)	106.8	18.0	102.0	21.7	92	0.7 - 2.9	1.00	0	36	0.	0.57		
CL	Pittsburg Silty Clay	118.9	13.5	105.4	11.5	52	1.0 - 3.0	0.92	31	650	-0.68	0.90	190	-0.81
CL	Pittsburg Silty Clay	118.9	13.5	109.1	14.3	71	1.0 - 6.0	1.50	17	760	-0.14	0.93	240	-0.21
CL	Pittsburg Silty Clay	118.9	13.5	109.0	16.8	83	1.0 - 6.0	1.30	6	430	0.10	0.93	115	0.10
CL	Pittsburg Silty Clay	118.9	13.5	112.7	11.5	63	1.0 - 6.0	1.80	24	2400	-0.74	0.92	740	-0.96
CL	Pittsburg Silty Clay	118.9	13.5	114.7	14.5	84	1.0 - 3.0	1.90	13	2000	-0.30	0.97	460	-0.64
CL	Pittsburg Silty Clay	118.9	13.5	108.8	8.71	43	1.0 - 6.0	1.50	32	8900	-1.10	0.94	1900	-1.1
CL	Pittsburg Silty Clay	118.9	13.5	119.3	11.7	77	1.0 - 6.0	3.30	18	5000	-0.28	0.95	1400	-0.33
CL	Sandy Clay (Birch Dam Core)	110.3	14.5	105.0	12.5	57	1.0 - 6.0	0.64	29	320	-0.21	0.80		
CL	Sandy Clay (Birch Dam Core)	110.3	14.5	105.0	14.5	66	1.5 - 6.0	0.50	25	190	0.02	0.81		
CL	Sandy Clay (Somerville Dam)	107.5	17.2	107.9	17.2	87	0.5 - 6.0	1.00	2	74	0.23	0.87		
CL	Sandy Clay (Somerville Dam)	107.5	17.2	107.2	17.0	74	0.5 - 6.0	1.00	1	68	-0.06	0.84		
CL	Sandy Clay (Somerville Dam)	107.5	17.2	102.6	20.0	88	0.5 - 6.0	0.45	1	27	0.18	0.85		
CL	Sandy Clay (Somerville Dam)	113.3	14.5	108.3	14.6	74	0.5 - 6.0	0.57	25	320	0.29	0.85		
CL	Sandy Clay (Somerville Dam)	95.7	23.3	96.5	23.2	89	0.5 - 6.0	1.50	4	200	0.29	0.89		
CL	Sandy Clay (Somerville Dam)	95.7	23.3	91.7	23.5	77	1.5 - 6.0	1.20	3	100	0.18	0.86		
CL	Sandy Clay (Somerville Dam)	95.7	23.3	90.8	26.7	87	0.5 - 6.0	0.64	1	53	0.14	0.90		

Table A.2. – Hyperbolic parameters for undrained conditions. From [24]. – Continued

Soil	Soil description	Compaction				Degree saturation	Stress range (TSF)	C (TSF)	Friction angle	K	n	R <sub>f</sub>	K <sub>b</sub>	m
		Max. dry unit wt. (lb/ft <sup>3</sup> )	Opt. w/c	Dry unit wt. (lb/ft <sup>3</sup> )	w/c									
CL	Sandy Clay (Somerville Dam)	110.7	15.0	111.8	15.1	86	0.5 - 6.0	0.84	22	160	0.34	0.78		
CL	Sandy Clay (Somerville Dam)	110.7	15.0	106.5	15.0	74	0.5 - 6.0	0.55	22	290	0.27	0.91		
CL	Sandy Clay (Somerville Dam)	107.5	16.8	100.5	13.5	58	0.5 - 6.0	0.78	28	680	-0.36	0.84		
CL	Sandy Clay (Somerville Dam)	107.5	16.8	106.5	13.3	66	0.5 - 6.0	1.50	25	600	0.18	0.68		
CL	Sandy Clay (Somerville Dam)	107.5	16.8	102.6	19.3	87	0.5 - 6.0	0.74	6	23	0.32	0.61		
CL	Sandy Clay (Somerville Dam)	107.5	16.8	106.7	16.7	85	0.5 - 6.0	0.91	18	280	0.60	0.93		
CL	Sandy Clay (Somerville Dam)	107.5	16.8	101.5	16.3	72	0.5 - 6.0	0.66	20	220	0.23	0.90		
CL	Sandy Clay (Somerville Dam)	106.1	17.2	105.0	18.6	89	0.5 - 6.0	1.30	8	140	0.20	0.84		
CL	Sandy Clay (Somerville Dam)	106.1	17.2	101.9	17.1	75	0.5 - 6.0	1.00	13	120	0.09	0.83		
CL	Sandy Clay (Somerville Dam)	106.1	17.2	103.0	19.7	89	0.5 - 6.0	0.80	2	47	0.33	0.82		
CL	Sandy Clay (Somerville Dam)	106.1	17.2	106.5	13.9	70	0.5 - 6.0	1.50	24	950	-0.15	0.90		
CL	Sandy Clay (Somerville Dam)	106.1	17.2	108.3	16.9	89	0.5 - 6.0	1.50	8	470	0.	0.95		
CL	Sandy Clay (Somerville Dam)	104.9	17.6	98.7	20.8	86	0.5 - 6.0	0.67	4	75	0.44	0.88		
CL	Sandy Clay (Somerville Dam)	104.9	17.6	104.9	14.8	72	0.5 - 6.0	1.80	23	840	-0.19	0.84		
CL	Sandy Clay (Somerville Dam)	104.9	17.6	101.2	17.4	76	0.5 - 6.0	1.20	12	270	0.06	0.87		
CL	Sandy Clay (Somerville Dam)	104.9	17.6	100.5	14.2	62	0.5 - 6.0	1.40	29	1100	-0.36	0.83		
CL	Sandy Clay (Somerville Dam)	104.9	17.6	104.4	17.5	84	0.5 - 6.0	1.40	13	410	0.15	0.87		
CL	Lean Clay (Clinton Dam)	103.0	21.2	98.0	24.0	92	1.0 - 5.0	0.77	2	57	0.43	0.86		
CL	Lean Clay (Clinton Dam)	105.0	20.2	99.7	22.9	91	1.0 - 3.0	0.97	1	110	0.43	0.90		
CL	Lean Clay (Clinton Dam)	101.0	20.1	99.1	22.7	90	2.0 - 6.0	1.10	2	100	0.27	0.89		
CL	Lean Clay (Clinton Dam)	101.0	20.1	98.1	23.9	90	2.0 - 6.0	0.99	1	160	0.54	0.97		
CL	Lean Clay (Clinton Dam)	101.0	20.1	98.9	22.7	90	2.0 - 6.0	1.10	3	130	0.46	0.91		
CL	Lean Clay (Clinton Dam)	102.0	19.9	96.8	22.7	83	2.0 - 6.0	0.78	2	53	0.41	0.85		
CL	Sandy Clay (Chatfield Dam)	104.0	19.3	97.6	23.4	90	6.0 - 10.0	1.20	0	240	0.	0.95		
CL	Sandy Clay (Chatfield Dam)	113.0	15.1	107.4	18.1	86	6.0 - 10.0	0.95	0	160	0.	0.93		
CL	Sandy Clay (Proctor Dam)	115.0	14.6	114.8	12.2	72	1.5 - 6.0	1.60	12	150	0.16	0.79		
CL	Silty Clay (Canyon Dam)	116.2	15.2	110.9	13.0	67	1.0 - 14.3	2.00	20	440	0.17	0.85		
CL	Silty Clay (Canyon Dam)	116.2	15.2	115.8	13.1	77	1.0 - 14.3	2.50	20	440	0.34	0.86		
CL	Silty Clay (Canyon Dam)	112.8	16.7	111.0	16.2	84	1.0 - 6.3	1.00	16	110	0.94	0.91		
CL	Silty Clay (Canyon Dam)	112.8	16.7	112.2	16.6	88	1.0 - 4.1	1.40	11	67	0.71	0.77		
CL	Silty Clay (Canyon Dam)	112.8	16.7	110.3	17.3	88	1.1 - 4.1	1.00	9	37	0.37	0.65		
CL	Silty Clay (Canyon Dam)	108.8	18.0	106.3	16.2	75	4.1 - 13.5	2.20	3	71	1.06	0.98		
CH	Fat Clay (Clinton Dam)	94.0	26.5	90.0	28.8	90	1.0 - 3.0	0.61	4	92	0.21	0.89		
CH	Fat Clay (Monroe Dam)	95.5	26.5	89.3	31.1	93	0.7 - 2.9	0.37	0	21	0.	0.65		
CH	Fat Clay (Monroe Dam)	95.5	26.5	92.6	28.6	93	0.7 - 2.9	0.51	1	67	0.02	0.79		
CH	Fat Clay (Monroe Dam)	100.0	22.7	96.4	26.5	94	1.1 - 2.9	0.63	1	65	0.14	0.77		
CH	Fat Clay (Chatfield Dam)	95.0	24.4	90.3	27.4	84	6.0 - 10.0	1.20	0	36	0.72	0.91		
CH	Fat Clay (Chatfield Dam)	95.0	24.4	90.7	24.4	76	6.0 - 10.0	1.50	2	52	0.66	0.89		

**APPENDIX B**  
**CALCULATIONS OF CAP PARAMETERS FOR OROVILLE DAM**



Calculate cap parameters for Oroville Dam

Parameters used in Hyporbolic model from Duncan, et. al (1980)

Element Group	c	$\phi$	K	n	$p_a$
2,9,10	0.	43.5	3780	0.19	2116
3,7,8	2640.	25.1	345.	0.76	
4,5	0.	43.5	3350.	0.19	

Needed for Cap Model

	LTYPE	T cut	$E_1$	$U_1$	CA	CB	CC	CR	CD	CW	XInt
2,9,10	1	0.0	12,789,911	0.25	28896	0.8	28896	4.76	0.001	0.001	-50050
3,7,8	1	0.0	4,772,073	0.25	28896	0.8	26825	8.13	0.001	0.001	-50050
4,5	1	0.0	11,334,531	0.25	28896	0.8	28896	4.76	0.001	0.001	-50050

1. LTYPE - use soil model = 1

2. T cut - use 0.0

3.  $E_1$

$$\text{use: } E_1 = K p_a (\sigma_3 / p_a)^n$$

Choose an average value of 1/2 height of maximum section

$$\sigma_1 = 130 \text{ lbs/ft}^2 \times 770/2 = 50050 \text{ lbs/ft}^2$$

$$\sigma_3 \text{ take} = 1/2 (\sigma_1) = 25025 \text{ lbs/ft}^2$$

$$E_1 = 3780 (2116) (25025/2116)^{0.19} = 127,89,411 \text{ lbs/ft}^2$$

$$E_1 = 345 (2116) (25025/2116)^{0.76} = 4,772,073 \text{ lbs/ft}^2$$

$$E_1 = 3350 (2116) (25025/2116)^{0.19} = 11,334,531 \text{ lbs/ft}^2$$

4.  $U_1$  take = 0.25

5. CA =  $J_{2D_{\max}}$

Take  $\sigma_1$  at bottom element of dam = 100100 lbs/ft<sup>2</sup>

$$\sigma_3 \text{ take} = 1/2 \sigma_1 = 50050$$

$$J_{2D} = 1/6 ( (\sigma_1 - \sigma_3)^2 + (\sigma_2 - \sigma_3)^2 + (\sigma_3 - \sigma_1)^2 )$$

$$(J_{2D_{\max}})^{1/2} = 28896 = CA$$

6. CB take = 0.8 from published results

7. CC - CA = Intercept at  $(J_{2D})^{1/2} = 0$  or k

$$k = \frac{3c}{9+12 \tan \phi} = \frac{3(2640)}{9+12 \tan (75.1)} = 2071.0$$

$$CC - CA = 2071 \quad CC = 30940$$

8. CR take as  $1/\alpha$

$$\alpha = \frac{\tan \phi}{9+12 \tan \phi} \quad \text{For}$$

$$\phi = 43.5 \quad \alpha = 6.210 \quad CR = 4.76$$

$$\phi = 25.1 \quad \alpha = 0.123 \quad CR = 8.13$$

9. CD take as 0.001

10. CW take as 0.001

11. XInt use  $\sigma_3$  at 1/2 height or 50050



### **Mission of the Bureau of Reclamation**

*The Bureau of Reclamation of the U.S. Department of the Interior is responsible for the development and conservation of the Nation's water resources in the Western United States.*

*The Bureau's original purpose "to provide for the reclamation of arid and semiarid lands in the West" today covers a wide range of interrelated functions. These include providing municipal and industrial water supplies; hydroelectric power generation; irrigation water for agriculture; water quality improvement; flood control; river navigation; river regulation and control; fish and wildlife enhancement; outdoor recreation; and research on water-related design, construction, materials, atmospheric management, and wind and solar power.*

*Bureau programs most frequently are the result of close cooperation with the U.S. Congress, other Federal agencies, States, local governments, academic institutions, water-user organizations, and other concerned groups.*

A free pamphlet is available from the Bureau entitled "Publications for Sale." It describes some of the technical publications currently available, their cost, and how to order them. The pamphlet can be obtained upon request from the Bureau of Reclamation, Attn D-822A, P O Box 25007, Denver Federal Center, Denver CO 80225-0007.